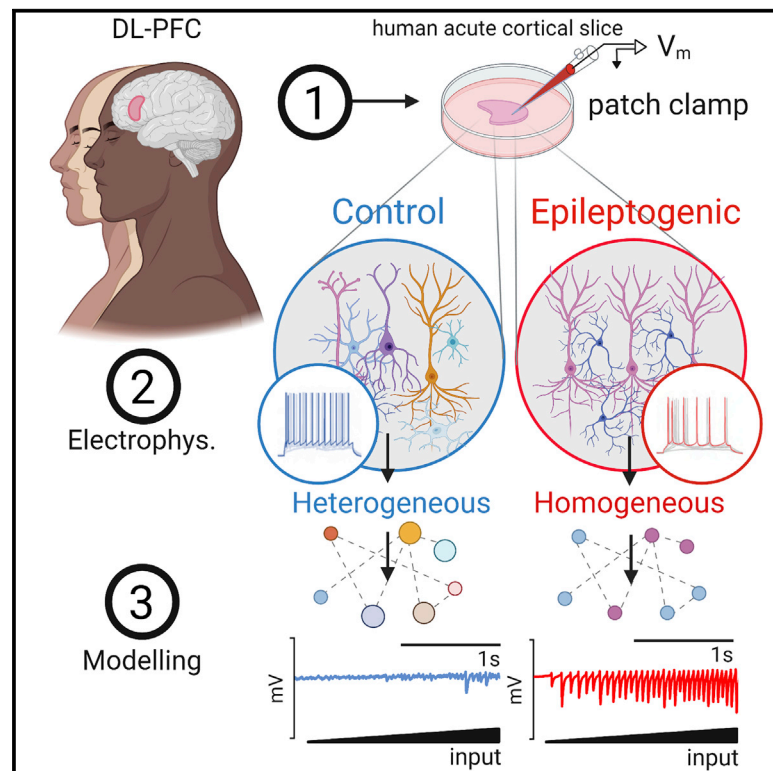


# Loss of neuronal heterogeneity in epileptogenic human tissue impairs network resilience to sudden changes in synchrony

## Graphical abstract



## Authors

Scott Rich, Homeira Moradi Chameh, Jeremie Lefebvre, Taufik A. Valiante

## Correspondence

jeremie.lefebvre@uottawa.ca (J.L.),  
taufik.valiante@uhn.ca (T.A.V.)

## In brief

Rich et al. demonstrate that neural heterogeneity is significantly reduced in epileptogenic human brain tissue. Implemented in computational and mathematical models, this homogenization renders neural circuits less resilient to sudden transitions analogous to seizure onset. These findings support the hypothesis that ictogenic dynamics accompany biophysical homogenization observed in epilepsy.

## Highlights

- Neural heterogeneity is significantly reduced in epileptogenic human cortex
- Heterogeneous model neural circuits are more resilient to seizure-like transitions
- Heterogeneity suppresses multistability in mean-field neural circuit approximations



## Article

# Loss of neuronal heterogeneity in epileptogenic human tissue impairs network resilience to sudden changes in synchrony

Scott Rich,<sup>1,9,11</sup> Homeira Moradi Chameh,<sup>1,9</sup> Jeremie Lefebvre,<sup>1,2,3,9,10,\*</sup> and Taufik A. Valiante<sup>1,4,5,6,7,8,9,10,\*</sup><sup>1</sup>Division of Clinical and Computational Neuroscience, Krembil Brain Institute, Toronto, ON M5T 1M8, Canada<sup>2</sup>Department of Biology, University of Ottawa, Ottawa, ON K1N 6N5, Canada<sup>3</sup>Department of Mathematics, University of Toronto, Toronto, ON M5S 1A1, Canada<sup>4</sup>Institute of Biomedical Engineering, University of Toronto, Toronto, ON M5S 1A1, Canada<sup>5</sup>Electrical and Computer Engineering, University of Toronto, Toronto, ON M5S 1A1, Canada<sup>6</sup>Institute of Medical Science, University of Toronto, Toronto, ON M5S 1A1, Canada<sup>7</sup>Division of Neurosurgery, University of Toronto, Toronto, ON M5S 1A1, Canada<sup>8</sup>Max Planck-University of Toronto Centre for Neural Science and Technology, University of Toronto, Toronto, ON M5S 1A1, Canada<sup>9</sup>Center for Advancing Neurotechnological Innovation to Application (CRANIA), University of Toronto, Toronto, ON M5S 1A1, Canada<sup>10</sup>These authors contributed equally<sup>11</sup>Lead contact\*Correspondence: [jeremie.lefebvre@uottawa.ca](mailto:jeremie.lefebvre@uottawa.ca) (J.L.), [taufik.valiante@uhn.ca](mailto:taufik.valiante@uhn.ca) (T.A.V.)<https://doi.org/10.1016/j.celrep.2022.110863>

## SUMMARY

A myriad of pathological changes associated with epilepsy can be recast as decreases in cell and circuit heterogeneity. We thus propose recontextualizing epileptogenesis as a process where reduction in cellular heterogeneity, in part, renders neural circuits less resilient to seizure. By comparing patch clamp recordings from human layer 5 (L5) cortical pyramidal neurons from epileptogenic and non-epileptogenic tissue, we demonstrate significantly decreased biophysical heterogeneity in seizure-generating areas. Implemented computationally, this renders model neural circuits prone to sudden transitions into synchronous states with increased firing activity, paralleling ictogenesis. This computational work also explains the surprising finding of significantly decreased excitability in the population-activation functions of neurons from epileptogenic tissue. Finally, mathematical analyses reveal a bifurcation structure arising only with low heterogeneity and associated with seizure-like dynamics. Taken together, this work provides experimental, computational, and mathematical support for the theory that ictogenic dynamics accompany a reduction in biophysical heterogeneity.

## INTRODUCTION

Epilepsy, the most common serious neurological disorder in the world (Reynolds, 2002), is characterized by the brain's proclivity for seizures, which exhibit highly correlated electrophysiological activity and elevated neuronal spiking (Jiruska et al., 2013). While the etiologies that predispose the brain to epilepsy are myriad (Jasper, 2012), the dynamics appear to be relatively conserved (Jirsa et al., 2014; Saggio et al., 2020), suggesting a small palette of candidate routes to the seizure state. One potential route to ictogenesis is disruption of excitatory/inhibitory balance (EIB), a possible "final common pathway" for various epileptogenic etiologies motivating decades of research into epilepto- and ictogenesis (Dehghani et al., 2016; Żiburkus et al., 2013). A disrupted EIB can impair the resilience of neural circuits to correlated inputs (Renart et al., 2010), a paramount characteristic of ictogenesis. In addition to EIB, biophysical heterogeneity also provides resilience to correlated inputs (Mishra and Narayanan, 2019).

Thus, EIB can be considered a synaptic mechanism for input decorrelation, while biophysical heterogeneity contributes to decorrelation post-synaptically.

Cellular heterogeneity is the norm in biological systems (Altschuler and Wu, 2010; Marder and Goaillard, 2006). In the brain, experimental and theoretical work has demonstrated that such heterogeneity expands the informational content of neural circuits by reducing correlated neuronal activity (Padmanabhan and Urban, 2010; Tripathy et al., 2013). Since heightened levels of firing and firing rate correlations hallmark seizures (Jirsa et al., 2014; Zhang et al., 2011), we hypothesize that epilepsy may be likened, in part, to pathological reductions in biological heterogeneity that impair decorrelation, and thus circuit resilience to information-poor (Trevelyan et al., 2013), high-firing (Jiruska et al., 2013), and highly correlated states (Zhang et al., 2011).

A number of pathological changes accompanying epileptogenesis can be recast as decreases in biological heterogeneity.



Losses of specific cell-types homogenize neural populations (Cossart et al., 2001; Cobos et al., 2005), down- or upregulation of ion channels homogenize biophysical properties (Arnold et al., 2019; Klaassen et al., 2006; Albertson et al., 2011), and synaptic sprouting homogenizes neural inputs (Sutula and Dudek, 2007). This recontextualizes epileptogenesis as a process associated in part with the progressive loss of biophysical heterogeneity.

To explore this hypothesis we combine electrophysiological recordings from human cortical tissue, computational modeling, and mathematical analysis to detail the existence and consequences of one reduction in biological heterogeneity in epilepsy: the decrease of intrinsic neuronal heterogeneity. We first provide experimental evidence for decreased biophysical heterogeneity in neurons within brain regions that generate seizures (epileptogenic zone) when compared to non-epileptogenic regions. These data constrain an exploration of the effects of heterogeneity in neural excitability on simulated brain circuits. Using a cortical excitatory-inhibitory (E-I) spiking neural network, we show that networks with neuronal heterogeneity mirroring epileptogenic tissue are more vulnerable to sudden shifts from an asynchronous to a synchronous state with clear parallels to seizure onset. Networks with neuronal heterogeneity mirroring non-epileptogenic tissue are more resilient to such transitions. These differing heterogeneity levels also underlie significant, yet counter-intuitive, differences in neural activation functions (i.e., frequency-current or FI curves) measured inside and outside the epileptogenic zone. Using mean-field analysis, we show that differences in the vulnerability to these sudden transitions and activation functions are both consequences of varying neuronal heterogeneities. Viewed together, our experimental, computational, and mathematical results support the hypothesis that biophysical heterogeneity enhances the dynamical resilience of neural networks while explaining how reduced diversity can predispose circuits to seizure-like dynamics.

## RESULTS

### Intrinsic biophysical heterogeneity is reduced in human epileptogenic cortex

In search of experimental evidence for reduced biophysical heterogeneity in epileptogenic regions, we utilized the rare access to live human cortical tissue obtained during resective surgery. Whole-cell current clamp recordings characterized the passive and active properties of layer 5 (L5) cortical pyramidal cells from these samples, a cell type we have shown to display notable biophysical heterogeneity (Moradi Chameh et al., 2021). Biophysical properties of neurons from epileptogenic frontal lobe cortex were contrasted to frontal lobe neurons of tumor patients, with no previous history of seizures, taken a distance from the tumor. Additionally, we obtained, from patients with mesial temporal sclerosis, recordings from neurons in non-epileptogenic middle temporal gyrus (MTG), which is the overlying cortex routinely removed to approach deep temporal structures. The MTG is a well-characterized part of the human brain, representing a common anatomical region from which non-epileptogenic brain tissue has been studied electrophysiologically and transcriptomically (Hodge et al., 2019; Moradi Chameh et al., 2021; Beaulieu-Laroche et al., 2018; Kalmbach et al.,

2021) and our primary source of non-epileptogenic neurons. We note that each of these studies classify these neurons as indicative of “seemingly normal” human neurons independent of the patients’ epilepsy or tumor diagnoses (i.e., a best-case control given limitations in obtaining human tissue).

While multiple sources of heterogeneity were recorded in a variety of physiological measurements (Figure S1), we concentrated on attributes of cellular heterogeneity that demonstrated significant differences between the epileptogenic and non-epileptogenic settings. The first was the distance to threshold (DTT) measured as the difference between the resting membrane potential (RMP) and threshold voltage (see Figure S1 for these measures presented individually). DTT displayed reduced variability (smaller coefficient of variation [CV];  $p = 0.04$ ; two sample coefficient of variation test) in neurons from epileptogenic frontal lobe ( $n = 13$ ,  $CV = 20.3\%$ ) compared to non-epileptogenic MTG ( $n = 77$ ,  $CV = 37.1\%$ ). A significant difference (smaller CV;  $p = 0.03$ ) was also seen when comparing epileptogenic frontal lobe to non-epileptogenic frontal lobe ( $n = 12$ ,  $CV = 40.8\%$ ). Meanwhile, the CVs were not significantly different when comparing non-epileptogenic MTG and non-epileptogenic frontal lobe ( $p = 0.7$ ). These features are more easily appreciated from the Gaussian fits of this data presented in Figure 1B. These results imply that the decrease in biophysical heterogeneity observed in epileptogenic cortex was not confounded by sampling from the temporal versus frontal lobe.

While our non-epileptogenic MTG population is larger, this is unavoidable given the availability of human cortical tissue and the additional efforts required to confirm the tissue’s epileptogenic nature (see discussion). Statistical tests accounting for unequal population sizes were used in comparing the population CVs and confirmed using the Krishnamoorthy and Lee test, via the R package *cvequality* (Marwick and Krishnamoorthy, 2019), which is robust to uneven sample numbers and small sample sizes (Krishnamoorthy and Lee, 2014). Additionally, the significant difference between the standard deviations (SDs) of the DTTs in non-epileptogenic MTG and epileptogenic frontal lobe ( $p = 0.03$ , Cohen’s  $d$  effect size = 0.5; F-test;  $SD = 7.8$  mV in non-epileptogenic MTG and  $SD = 4.4$  mV in epileptogenic frontal lobe) that is implemented in our models has a “moderate” effect size. Finally, we confirmed that the measured heterogeneities are not biased by variability between patients (Figure S2), a finding supported by recent multi-patch data in human cortex showing that biophysical properties demonstrate smaller between-subject than within-subject variability (Planert et al., 2021).

The second measure of cellular excitability that demonstrated significant difference between groups was the FI curve (i.e., activation function), which captures the firing rate ( $F$ ) as a function of input current ( $I$ ). The FI curve of the population of neurons from the epileptogenic zone displayed qualitative and quantitative differences compared to neurons from both non-epileptogenic MTG and frontal lobe (Figure 1C). Interestingly, the FI curve shows that pyramidal cells from the epileptogenic zone require more input current to induce repetitive firing and have overall decreased firing rates for all input currents ( $p = 0.03$  when comparing to non-epileptogenic frontal lobe at 200 pA,  $p = 0.02$  when comparing to non-epileptogenic frontal lobe at

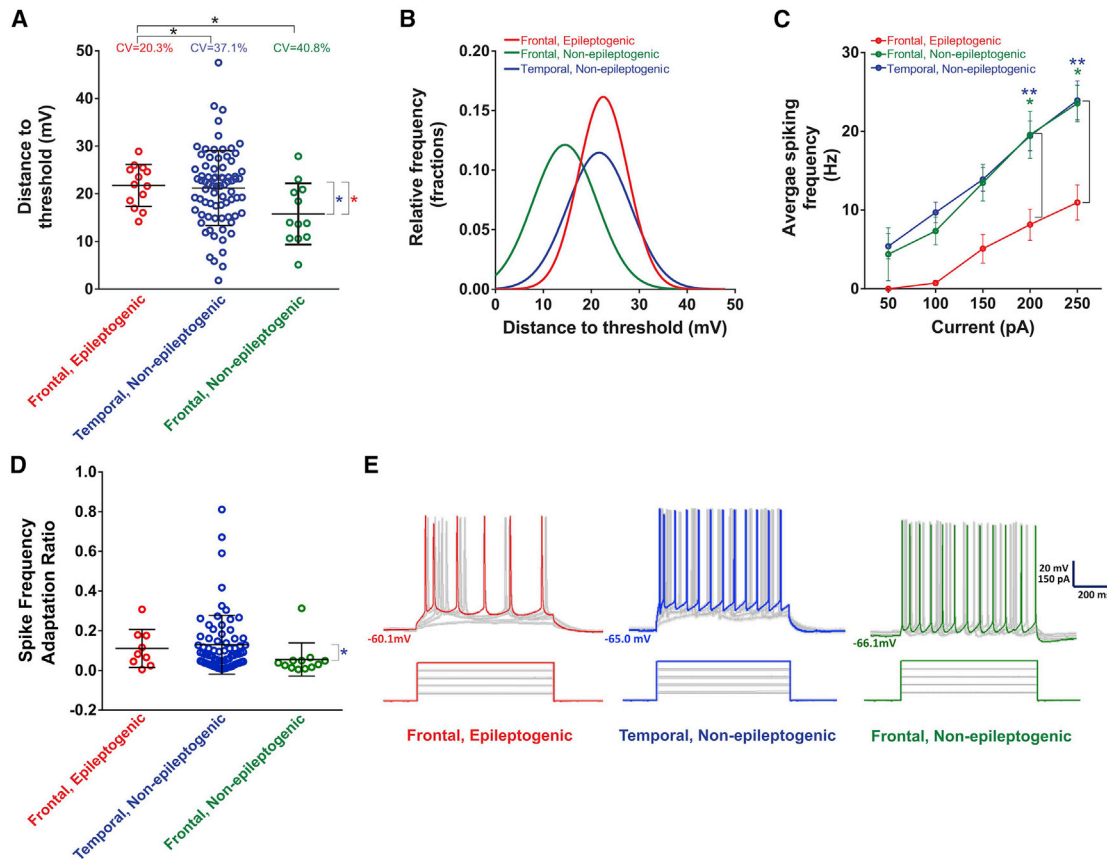


**Figure 1.** *In vitro* human tissue recordings reveal significantly different electrophysiological heterogeneity between epileptogenic and non-epileptogenic populations

(A) The coefficient of variation (CV) in the distance to threshold (DTT) is significantly larger in both the temporal, non-epileptogenic (i.e., non-epileptogenic MTG;  $n = 77$ ) and frontal, non-epileptogenic (i.e., non-epileptogenic frontal lobe;  $n = 12$ ) populations compared to the frontal, epileptogenic (i.e., epileptogenic frontal lobe;  $n = 13$ ) population ( $p = 0.04$  to temporal, non-epileptogenic,  $p = 0.03$  to frontal, non-epileptogenic; two sample coefficient of variation test). The CV measure is implemented considering the significantly reduced mean DTT in frontal, non-epileptogenic data compared with the other two populations ( $p = 0.01$  for both comparisons; non-parametric Mann-Whitney test). We compare the frontal, epileptogenic and temporal, non-epileptogenic populations computationally given their similar mean DTT ( $p = 0.7$ ). Plotted bars indicate mean  $\pm$  standard deviation (SD).

(B) An alternative visualization of the DTT distributions via fit Gaussian probability density functions. All three datasets were deemed normal after passing both the Shapiro-Wilk and D'Agostino-Pearson omnibus normality test with  $\alpha = 0.05$ .

(C) Neurons from non-epileptogenic populations show similar, linear activation functions (i.e., FI curves). Firing frequency is significantly lower in the frontal, epileptogenic population for a 200-pA injection compared to the temporal, non-epileptogenic ( $p = 0.009$ ; two-way ANOVA-Tukey's multiple comparison test) and frontal, non-epileptogenic ( $p = 0.03$ ) populations, as well as for a 250-pA injection compared to the temporal, non-epileptogenic ( $p = 0.002$ ) and frontal, non-epileptogenic ( $p = 0.02$ ) populations. Plotted bars indicate mean  $\pm$  standard error measure (SEM).

(D) All three populations show a similar spike frequency adaptation ratio (see details in STAR Methods), with the only significant difference being between the means from the frontal, non-epileptogenic and temporal, non-epileptogenic populations ( $p = 0.01$ ; one-way ANOVA post hoc with Dunn's multiple comparison test). Plotted bars indicate mean  $\pm$  SD.

(E) Example cell voltage responses following depolarizing current injections (50–250 pA) from all three populations, as used to calculate the FI curve (colors denote population as in previous panels). See also Figures S1 and S2.

250 pA,  $p = 0.009$  when comparing to non-epileptogenic MTG at 200 pA, and  $p = 0.002$  when comparing to non-epileptogenic MTG at 250 pA; two-way ANOVA-Tukey's multiple comparison test). This non-linear behavior is in strong contrast to the activation functions measured in non-epileptogenic zones, characterized by both higher and more linear changes in firing rates. All three populations show a similar spike frequency adaptation ratio (Figure 1D), including no significant difference between epileptogenic frontal lobe and non-epileptogenic MTG (the re-

gions focused on in our modeling), indicating that differences in the FI curve are not due to differing adaptation ratios. Example firing traces from each population (in response to each of the current steps used in FI curve generation; note that the spike frequency adaptation ratio is calculated from one of these steps, chosen as described in the STAR Methods for each individual neuron) are found in Figure 1E. This increased excitability of the non-epileptogenic populations appears contradictory to the understanding of seizure as a hyperactive brain state,

although some prior studies have hinted at this phenomenon (Colder et al., 1996; Schwartzkroin et al., 1983); additionally, the significantly increased first-spike latency in our epileptogenic population (Figure S1C) is further evidence for the decreased single-cell excitability of neurons in this population. We further investigate this in the context of biophysical heterogeneity below.

FI curves from epileptogenic neurons also demonstrated decreased variability: the SDs of the frequencies in the epileptogenic population are significantly lower compared to the temporal, non-epileptogenic population at 150 pA ( $p = 0.02$ , Levene's test) and at 200 pA ( $p = 0.03$ ), and to the frontal, non-epileptogenic population at 200 pA ( $p = 0.03$ ). Furthermore, the higher input current required to elicit repetitive spiking in our epileptogenic population can be contextualized as a homogenizing feature, as neurons will respond homogeneously (i.e., without spiking) to a larger range of inputs. The smaller slope of the epileptogenic FI curve has a similar effect when repetitive spiking occurs, as changes in the input current will yield smaller changes in the output firing frequency. These findings showcase an additional pattern of decreased heterogeneity in epileptogenic neurons' spiking behavior.

### Spiking E-I neural networks with epileptogenic levels of excitatory heterogeneity are more vulnerable to sudden changes in synchrony

Given these experimental results, we next computationally explored the effects of the observed differences in biophysical heterogeneity on the transition to a synchronous state akin to the transition to seizure (Zhang et al., 2011). We developed a spiking network model of a cortical microcircuit comprised of recurrently connected excitatory and inhibitory neurons (see details in STAR Methods), motivated in part by the long history of seizure modeling (Kramer et al., 2005; Jirsa et al., 2014) and previous models of decorrelated activity in the cortex (Vogels and Abbott, 2009; Renart et al., 2010; Ostojic, 2014). Our choice of model parameters (see details in STAR Methods) positioned the system near a tipping point at which synchronous activity might arise (Jadi and Sejnowski, 2014a, 2014b; Neske et al., 2015; Rich et al., 2020b) in order to determine the effects of cellular heterogeneity on this potential transition.

We subjected these networks to a linearly increasing external drive to the excitatory cells. This allowed us to observe the dynamics and stability of the asynchronous state, known to be the physiological state of the cortex (Vogels and Abbott, 2009; Renart et al., 2010; Ostojic, 2014), by determining how vulnerable the network is to a bifurcation forcing the system into a state of increased synchrony and firing. A biological analog for this paradigm would be an examination of whether induced hyperexcitability might drive the onset of seizure-like activity *in vitro*, although such perturbations can more easily be performed continuously (i.e., our linearly increasing external drive) *in silico*.

To facilitate implementing experimentally derived heterogeneities in our model, we compared epileptogenic frontal lobe with non-epileptogenic MTG given their similar mean DTT values ( $p = 0.7$ , non-parametric Mann-Whitney test; mean = 21.2 mV for non-epileptogenic MTG and mean = 21.7 mV for epileptogenic frontal lobe). These populations display significantly different

SDs in their DTT values (reported above). Given the definition of our neuron model (rheobases sampled from a normal distribution with mean 0; see details in STAR Methods), we implement differing heterogeneities by sampling rheobase values for our neural populations from Gaussian distributions with these varying SDs. In this model, the term rheobase refers to the inflection point of the model neuron's activation function (see STAR Methods). Heterogeneity in this mathematically defined rheobase is the *in silico* analog of heterogeneity in the DTT (i.e., the distribution of rheobases in Figures 2C and 2D corresponds to a horizontal shift to a mean of 0 of the DTT distributions in Figure 1B).

The rheobase heterogeneity was parameterized by the SD  $\sigma_e$  for excitatory neurons and  $\sigma_i$  for inhibitory neurons (see diagrams in Figures 2A and 2B). This resulted in diversity in the neurons' activation functions and aligned the variability in their excitabilities with that measured experimentally. We refer to such rheobase heterogeneity simply as heterogeneity in the remainder of the text. Models with non-epileptogenic (high  $\sigma_e = 7.8$  mV; Figure 2E) and epileptogenic (low  $\sigma_e = 4.4$  mV; Figure 2F) excitatory heterogeneity with identical inhibitory heterogeneity ( $\sigma_i = 10.0$  mV) exhibit distinct behaviors. With low excitatory heterogeneity, a sharp increase in excitatory synchrony associated with increased firing rates is observed. In contrast, when the excitatory heterogeneity was high, both synchrony and firing rates scaled linearly with input amplitude.

We further investigated the respective roles of excitatory versus inhibitory heterogeneity in these sudden transitions. With non-epileptogenic excitatory heterogeneity (high  $\sigma_e$ ), increases in excitatory synchrony, excitatory firing rates, and inhibitory firing rates were all largely linear regardless of whether  $\sigma_i$  was low (Figure 3A) or high (Figure 3B). Conversely, with excitatory heterogeneity reflective of epileptogenic cortex (low  $\sigma_e$ ), synchronous transitions were observed for both low (Figure 3C) and high (Figure 3D) levels of  $\sigma_i$ . This transition is of notably higher amplitude when  $\sigma_i$  is low, indicative of differing underlying dynamical structures driven by  $\sigma_i$ .

Limitations inherent in performing patch-clamp experiments in human cortical tissue prevented the direct measurement of DTT variability in human inhibitory interneurons. To circumvent this, we first studied a range of inhibitory DTT variability aligning with that measured in pyramidal neurons, and then we systematically varied and extended this range to account for the possibility of increased heterogeneity among the interneuronal population (Cossart, 2011; Huang and Paul, 2019). This enabled the characterization of the contribution of both excitatory and inhibitory heterogeneity to the onset of seizure-like behavior across physiologically relevant ranges of  $\sigma_e$  and  $\sigma_i$ . Exploring this range of  $\sigma_i$  values revealed dichotomous dynamics at low and high heterogeneities (Figure S3), of which we illustrate exemplars in Figures 3 and 4.

### Dynamical differences in networks with varying levels of heterogeneity are explained by their distinct mathematical structures

To gain deeper insight into the effect of heterogeneity at a potential transition to synchrony, we derived and analyzed mathematically the mean-field equations associated with our network

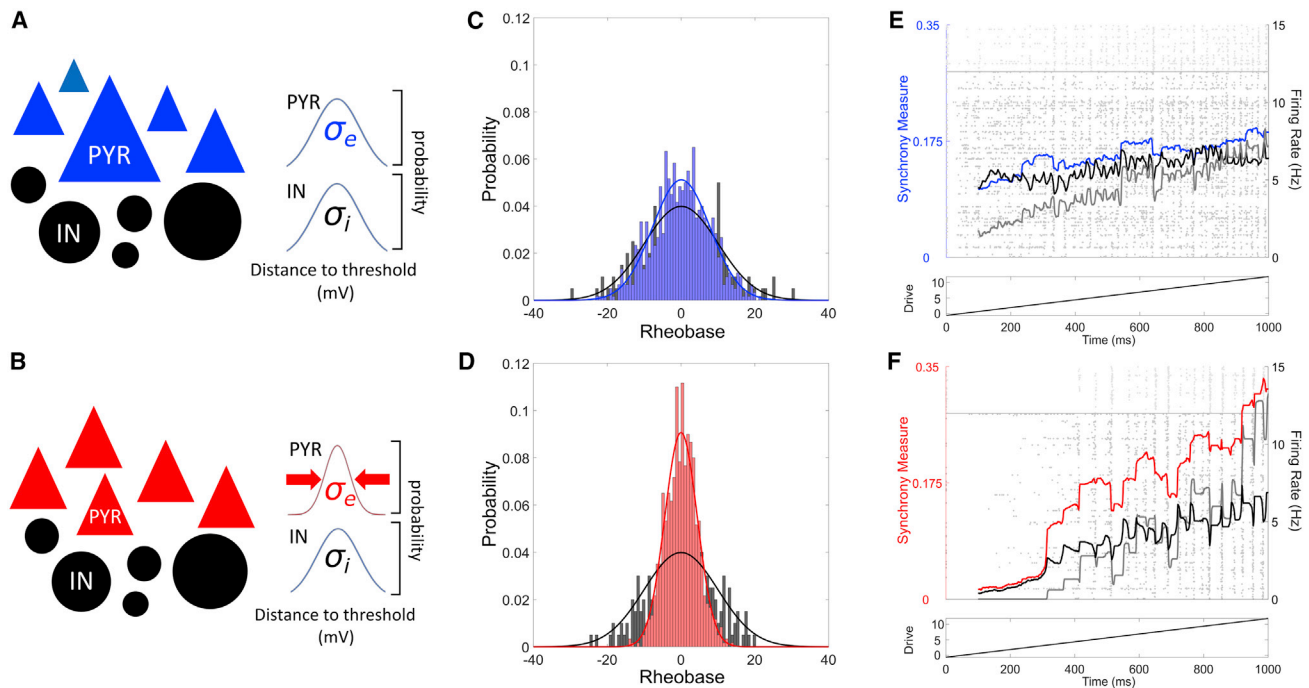


**Figure 2. Experimentally observed decreases in heterogeneity among excitatory cells promote ictogenic-like transitions in E-I spiking neural network models**

(A and B) Schematic representation of model spiking E-I networks, with pyramidal neurons represented as triangles and interneurons as circles. Blue neurons represent non-epileptogenic (i.e., high) levels of heterogeneity (see also the variable neuron sizes), while red neurons represent epileptogenic (i.e., low) levels of heterogeneity (see also the similar neuron sizes). This color schema is maintained in the remaining figures. Here, the inhibitory (black neurons) heterogeneity is set at a moderate value among the range studied ( $\sigma_i = 10.0$  mV), while  $\sigma_e = 7.8$  mV in (A) and  $\sigma_e = 4.4$  mV in (B).

(C and D) Visualizations of the distribution of model rheobases, with the solid curve (red or blue for excitatory neurons, black for inhibitory neurons) illustrating the Gaussian function, and the corresponding histogram illustrating the example random distribution underlying the simulations in this figure.

(E and F) Example simulations with a linearly increasing excitatory drive. Background: raster plot of network activity, with each circle representing the firing of an action potential of the associated neuron (excitatory neurons below horizontal line, inhibitory neurons above). Foreground: quantifications of network activity taken over 100-ms sliding time windows, with the excitatory synchrony quantified by the synchrony measure in blue or red (left axis), as well as excitatory (black) and inhibitory (gray) population firing rates (right axis). Bottom: drive ( $I_e(t)$ ) to the excitatory population.

model (see STAR Methods). Specifically, we calculated and classified the fixed points of mean-field equations for different values of  $\sigma_e$  and  $\sigma_i$  for the range of drives studied in the spiking networks. The fixed point(s) of the mean-field (for the excitatory population activity,  $U_e$ ) are plotted in the second row of each panel in Figure 4. These values correspond to population averages of the (unitless) membrane potential analog taken across the individual units in our spiking networks ( $u_e^i$ ). We then performed linear stability analysis for those fixed points, extracting eigenvalues that determine the fixed points' stability, and how it might change as input drive is varied. The dampening rate represents the speed at which the system is either repelled from or returns to its fixed point(s) and thus classifies their stability (i.e., the real components of eigenvalues associated with each fixed point). The dampening rate is plotted in the row below the fixed points, followed by the frequency associated with fixed points with imaginary eigenvalues (i.e., the imaginary components of the eigenvalues).

These mean-field analyses confirm that both excitatory and inhibitory heterogeneity have notable impacts on changes in network dynamics analogous to seizure onset. In the top row of each panel in Figure 4, we present quantifications of our

spiking network dynamics as in Figure 3, but averaged over 100 independent simulations. In the presence of high heterogeneity (whenever  $\sigma_e$  and/or  $\sigma_i$  are large, i.e., Figures 4A, 4B, and 4D), increased drive results in a smooth and approximately linear increase in both mean activity and synchrony. The mean-field analyses of the associated systems reveal a single fixed point, whose value increases monotonically with drive.

The similar dynamics in these scenarios are reflected by their stability properties. When either or both of the heterogeneities are high (Figures 4A, 4B, and 4D), the mean-field analyses reveal a single, stable fixed point and the absence of bifurcations. Oscillatory behavior arises from the interaction between noise and stable oscillatory fixed points yielding quasi cycles (Boland et al., 2008), with the development of synchrony occurring gradually.

In contrast to these cases, spiking networks with low heterogeneity (low  $\sigma_e$  and  $\sigma_i$ ; Figure 4C) exhibit sudden increases in mean activity and synchrony. The associated mean-field system displays multistability: it possesses multiple fixed points. As the input drive increases, two of these fixed points coalesce and disappear via a saddle-node bifurcation (Chow and Hale, 2012). The system's mean activity is thus suddenly drawn

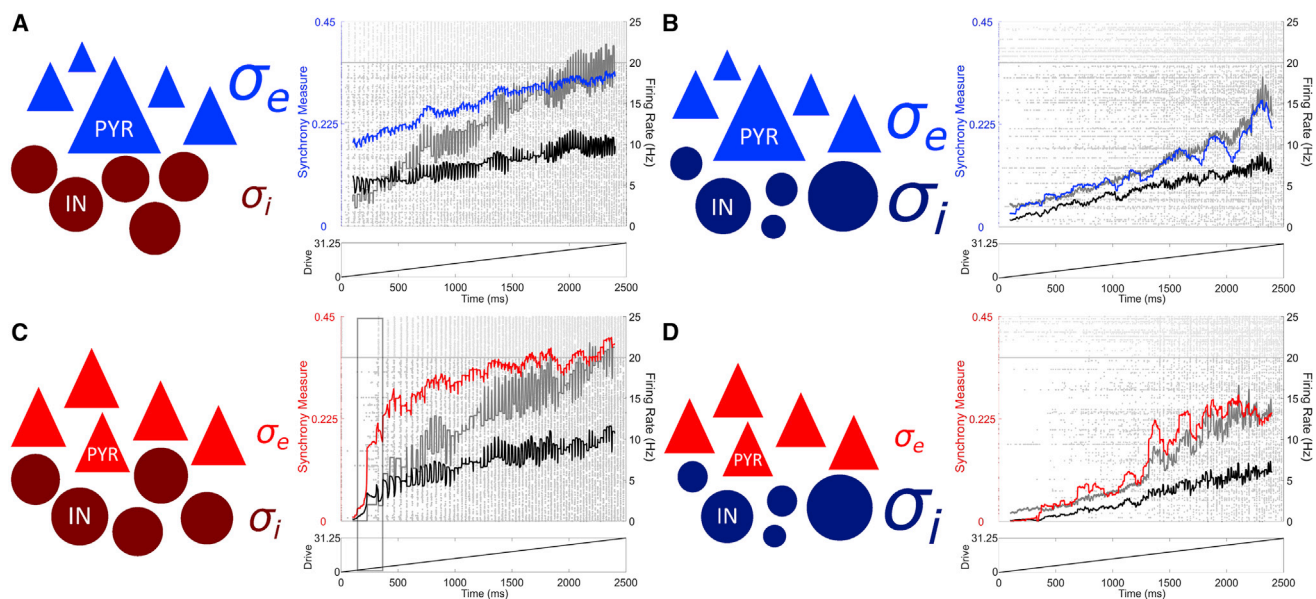


**Figure 3. Effects of varied inhibitory heterogeneity on sudden transitions into synchrony in E-I spiking neural network models**

Schematics and single simulation visualizations following the conventions of Figure 2 (with inhibitory heterogeneity reflected by darker shaded blue and red neurons), now shown for four combinations of excitatory and inhibitory heterogeneities:  $\sigma_e = 7.8$  mV and  $\sigma_i = 2.5$  mV in (A),  $\sigma_e = 7.8$  mV and  $\sigma_i = 16.75$  mV in (B),  $\sigma_e = 4.4$  mV and  $\sigma_i = 2.5$  mV in (C), and  $\sigma_e = 4.4$  mV and  $\sigma_i = 16.75$  mV in (D). Relative sizes of  $\sigma_e$  and  $\sigma_i$  represent the relative heterogeneity levels. Transitions into high levels of excitatory synchrony are seen in (C) and (D), with the transition in (C) yielding a notably higher level of synchrony (highlighted by the gray box) and occurring much more abruptly. Meanwhile, changes in the dynamics of (A) and (B) are largely linear, with the excitatory synchrony consistently lower when both excitatory and inhibitory heterogeneities are at their highest in (B). See also Figure S3.

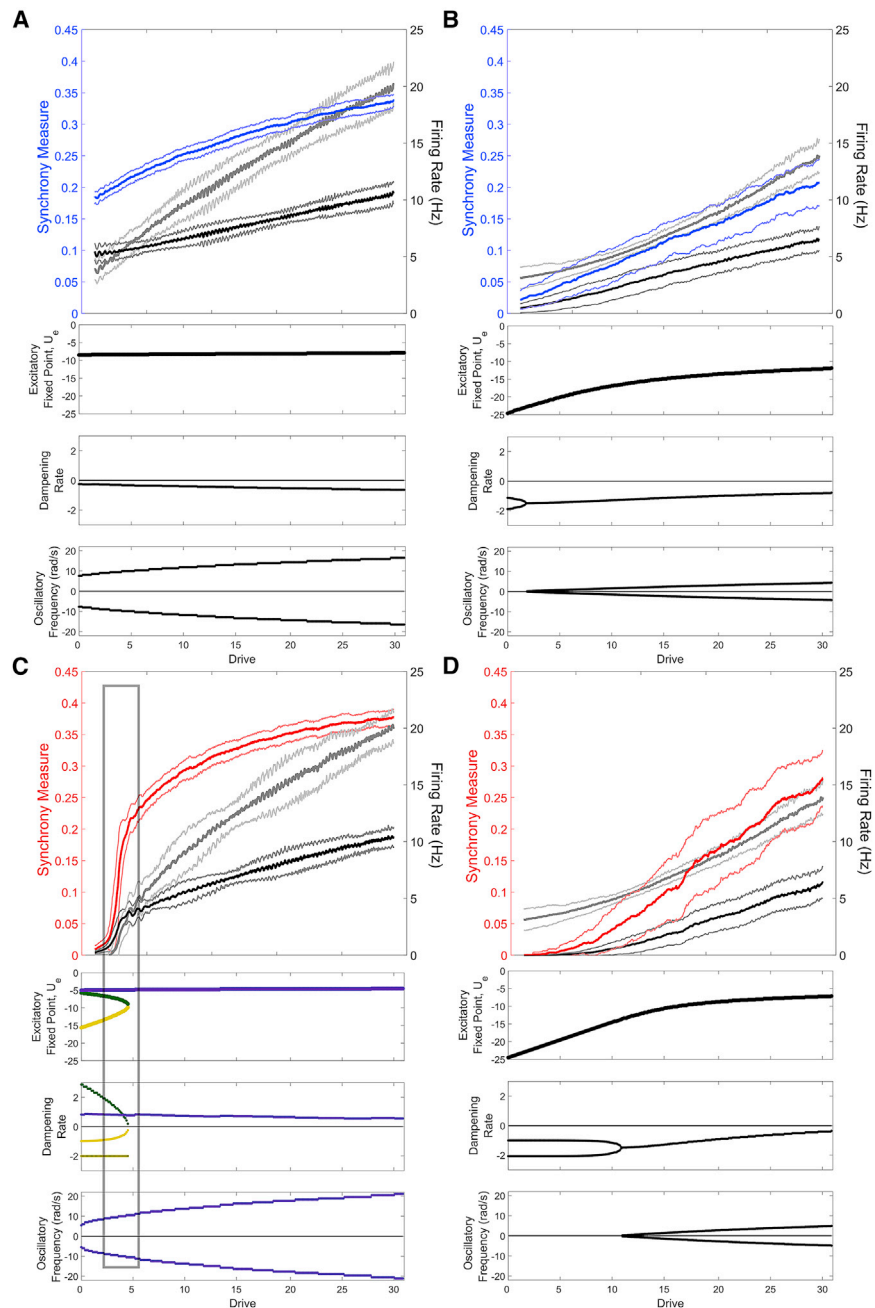
toward a preexisting large-amplitude limit cycle. This transition occurs at a drive corresponding with the sudden increase in synchrony and mean activity seen in the spiking network. In the mean-field system, the frequency of resulting oscillations is faster compared to the high heterogeneity scenarios, further emphasizing the uniqueness of the dynamical system with low heterogeneity.

We note that the more notable inter-trial variability in Figure 4D (as illustrated by the fainter  $\pm$  SD curves) results from the variable (yet gradual) onset of increased synchrony, in contrast to the transition in Figure 4C that reliably occurs at a specific drive. The different timings of the onset of synchrony in each independent simulation yield oscillations at different relative phases, which explains why oscillations are not observed in our averaged firing rate measures displayed in Figure 4 (notably, such oscillations are subtle even in the single simulation visualizations of Figure 3 given the 100-ms sliding time window); rather, the presence of oscillatory activity is demarcated by a notable increase in the mean synchrony measure.

In our mathematical analyses, we focus on characterizing the system's fixed points and inferring from them the presence of oscillatory behavior associated with limit cycles. Directly identifying such limit cycles is a mathematically arduous process (Savov and Todorov, 2000) unnecessary for the conclusions drawn from our analyses. However, considering the behavior of our spiking networks remains "bounded" (see Figure S3B), we can confidently infer that such limit cycles exist, as is typical when a supercritical Hopf bifurcation yields an unstable fixed point.

To facilitate the comparison of our spiking networks with our mean-field calculations, we developed a bifurcation measure (see STAR Methods) quantifying the tendency for sudden (but persistent) changes in the activity of the spiking network. Higher values of this measure indicate the presence of a more abrupt increase in the quantification of interest as the drive increases. Given the more subtle qualitative difference in the firing rates in our spiking networks, we applied the bifurcation measure to the excitatory firing rate ( $B_e$ ) for the four combinations of  $\sigma_e$  and  $\sigma_i$  examined in Figure 4. This revealed more sudden changes with low  $\sigma_e$  and  $\sigma_i$  ( $B_e = 0.1050$ ) as opposed to any other scenario (high  $\sigma_e$ , low  $\sigma_i$ ,  $B_e = 0.0416$ ; high  $\sigma_e$ , high  $\sigma_i$ ,  $B_e = 0.0148$ ; low  $\sigma_e$ , high  $\sigma_i$ ,  $B_e = 0.0333$ ) where the transition is smoother. This analysis indicates that the dynamical transition present in Figure 4C is not only distinctive in the magnitude of the synchronous onset, but also in an associated sudden increase in firing rates.

Since the seizure state is typified both by increased synchrony and firing rates (Jiruska et al., 2013; Zhang et al., 2011), this analysis confirms that the sharp transition in these quantities only observed in spiking models with low heterogeneity is driven by a saddle-node bifurcation (Figure 4C). These results echo other seizure modeling studies showcasing that ictogenic transitions can arise driven by mathematical bifurcations, and specifically the observation that saddle-node bifurcations underlie abrupt seizure-onset dynamics (Kramer et al., 2005; Jirsa et al., 2014; Saggio et al., 2020). As a corollary, high heterogeneity improves network resilience to sudden changes in synchrony by preventing multistability and fostering gradual changes in network firing rate and oscillatory behavior.



### Asymmetric effects of excitatory and inhibitory heterogeneity

Figure 4 highlights distinct effects of excitatory versus inhibitory heterogeneity on the onset of synchrony in spiking networks and the structure of mean-field systems (see the differences between Figures 4A and 4C). To clarify these effects, we explored a larger parameter space of  $\sigma_e$  and  $\sigma_i$ , as shown in Figure S3. For each heterogeneity combination, we applied the bifurcation measure to excitatory synchrony ( $B$ , hereafter referred to simply as the bifurcation measure; see details in STAR Methods), which quantifies the abruptness of increased network synchrony in

### Figure 4. Effects of heterogeneity on spiking network dynamics is explained by stability analysis of mean-field equations

Panels correspond to heterogeneity levels studied in Figure 3. Top row: measures of spiking network dynamics (as seen in Figures 2 and 3) averaged over 100 simulations (dark curve = mean, lighter curve =  $\pm$  one SD). Remaining rows: results of stability analysis on mean-field equations corresponding with these networks visualized via the fixed point of mean excitatory activity (top), and the dampening rate and oscillatory frequency associated with each fixed point. Green and gold coloring are used to differentiate the three distinct fixed points in (C), while the stability of fixed points is color coded (purple = unstable, i.e., positive dampening rate; black = stable, i.e., negative dampening rate). Notably, only in (C), where both heterogeneity levels are low, do we see multiple fixed points and a saddle-node bifurcation that occurs at a value of the drive corresponding with the sudden transition in spiking networks (highlighted by the gray box). See also Figures S4–S8.

response to a changing network drive. This exploration confirms the asymmetric effect of excitatory and inhibitory heterogeneity on these sudden transitions, with a moderate value of  $B$  for low  $\sigma_e$  and high  $\sigma_i$  but a minimal value of  $B$  for high  $\sigma_e$  and low  $\sigma_i$ , comporting with patterns observed in previous computational literature (Mejias and Longtin, 2014).

Similar asymmetry is seen in our spiking network dynamics ( $B$  in Figure S3A and the synchrony measure  $S$  in Figure S3B) and our mean-field systems (the bolded regimes of networks exhibiting multistability in Figure S3A and networks exhibiting an unstable fixed point in Figure S3B). We show an example visualization of the fixed points and their classifications in Figure S4. Figure S5 shows the details of the determination of fixed point stability in Figure S3B.

We further used the bifurcation measure to test whether the asymmetric effects of excitatory and inhibitory heterogeneity are generalizable and confirm our system's robustness.

In Figure S6 we show the pattern followed by  $B$  is robust to changes in connectivity density. In the four exemplar cases highlighted in Figures 3 and 4 the dynamics are robust for reasonable changes to the primary parameters dictating our network topology, as shown in Figure S7, and similar robustness in the bifurcation structure of the associated mean-field systems is shown in Figure S8.

This analysis shows that notable decreases in  $B$  occur at higher values of  $\sigma_i$  than they do for  $\sigma_e$ , a result that has important implications for our understanding of the potentially differing



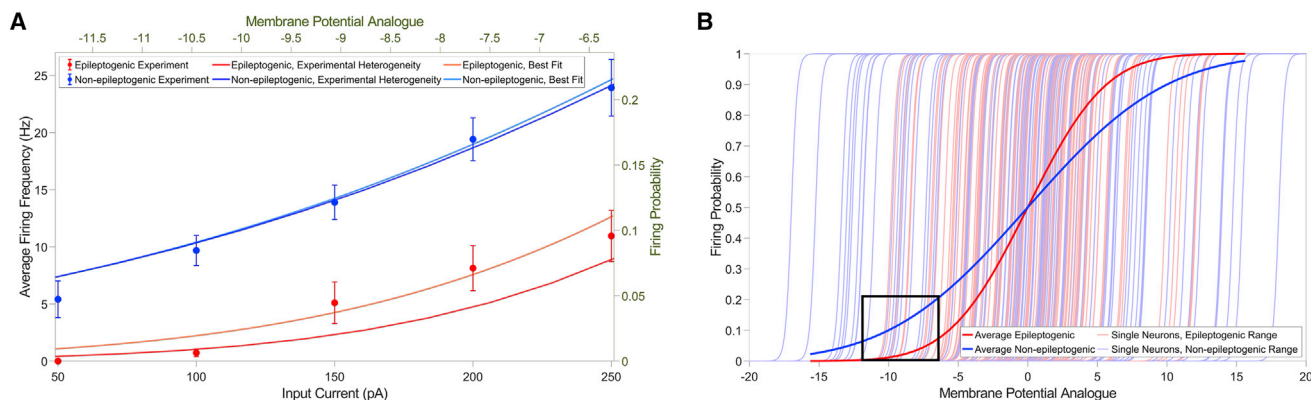


**Figure 5. Differing levels of neuronal heterogeneity explain population activation function differences observed experimentally between epileptogenic and non-epileptogenic cortex**

(A) Experimentally observed firing frequencies plotted against input current (left and bottom axes, mean  $\pm$  SEM) for epileptogenic frontal lobe (red) and non-epileptogenic MTG (blue) tissue (as shown previously in Figure 1C), visualized against an analogous measure of the relationship between population activity (firing probability) and drive (membrane potential analogue) in our neuron models (right and top axes, details in STAR Methods). The shape of the curve for the heterogeneity value derived from epileptogenic tissue experimentally (red,  $\sigma_e = 4.4$ ) qualitatively matches the experimental data, and a best fit (light red,  $\sigma_e = 5.03$ ,  $r^2 = 0.94$ ) is obtained with a similarly low heterogeneity value. In contrast, the curve associated with the heterogeneity value derived from non-epileptogenic tissue experimentally (blue,  $\sigma_e = 7.8$ ) closely matches the experimental data from non-epileptogenic tissue and is nearly identical to the best fit (light blue,  $\sigma_e = 7.77$ ,  $r^2 = .98$ ).

(B) A visualization of the entirety of the sigmoidal input-output relationship for our neuron models, with the regime compared to experimental data in (A) in a black box. Fainter curves represent input-output relationships for individual neurons, either epileptogenic (red) or non-epileptogenic (blue): the wider variability in the blue curves yields the flatter sigmoid representing the population activation function for our non-epileptogenic heterogeneity value, and vice-versa for the red curves associated with the epileptogenic heterogeneity value.

roles of excitatory and inhibitory heterogeneity in seizure resilience. When the loss of specific interneuron types in some epilepsies (Cossart et al., 2001; Cobos et al., 2005) and increases in inhibition (Klaassen et al., 2006) are viewed as homogenizing changes, these computational predictions may help reconcile how both increases and decreases in inhibition may be destabilizing to neuronal circuits.

### Differences in population-averaged activation functions explained by differences in neuronal heterogeneity

Finally, we return to the counter-intuitive differences in activation functions measured experimentally. As noted previously, the population of neurons from epileptogenic tissue exhibited qualitatively and quantitatively different activation functions via non-linear and hypo-active firing responses (Figure 1C).

To understand if heterogeneity accounts for these observations, we computed analytically the averaged activation functions of the excitatory populations in our model networks. In Figure 5A, the experimentally derived firing frequencies from epileptogenic frontal lobe and non-epileptogenic MTG are plotted alongside activation functions of our model populations. For low heterogeneity, the model population's activation function captured both the non-linear and low firing rate responses measured experimentally for neurons in the epileptogenic zone. The increased excitability and linearity seen experimentally in non-epileptogenic tissue were captured by the averaged activation function for our more heterogeneous model population. This comparison is appropriate considering the FI curve data from Figure 1C is averaged over the populations of interest, and is thus analogous to the population activation function of our model neurons.

To quantitatively support this correspondence, we found the values of  $\sigma_e$  that best fit our experimental data using a non-linear least squares method (see details in STAR Methods). The data from epileptogenic frontal lobe was best fit by an activation function (see Equation 12) with  $\sigma_e = 5.0$  mV ( $r^2 = 0.94$ ), while the data from non-epileptogenic MTG was best fit by an activation function with  $\sigma_e = 7.8$  mV ( $r^2 = 0.98$ ). The close match between the best-fit values and the experimentally observed heterogeneity values means the features of our epileptogenic (resp. non-epileptogenic) activation curves are captured by neural populations with low (resp. high) heterogeneity.

This somewhat counter-intuitive result is explained by the linearizing effect that increased heterogeneity, and noise more generally, has on input-output response functions (Mejias and Longtin, 2014; Lefebvre et al., 2015). This effect is illustrated in Figure 5B. The bolded sigmoids represent the averaged activity of the entire population of heterogeneous neurons alongside individual activation functions (fainter sigmoids). Increased (resp. decreased) variability dampens (resp. sharpens) the averaged response curve for the non-epileptogenic (resp. epileptogenic) setting. Such variability-induced linearization raises the excitability at low input values, corresponding with the dynamics highlighted in Figure 5A. Figure 5 illustrates that our model predicts significant differences in the activation function between epileptogenic and non-epileptogenic tissue, and that heterogeneity, or lack thereof, can explain counter-intuitive neuronal responses. However, these differences are not necessarily reflected in network dynamics, as illustrated by the similar network firing rates in Figures 4A and 4C at high levels of drive. In the context of seizure, this implies that excessive synchronization of a neural population need *not* be exclusively associated

with increased excitability as represented by a lower minimum input to elicit repetitive firing or a higher firing rate of the population of isolated neurons.

## DISCUSSION

In this work, we propose that neuronal heterogeneity may serve an important role in generating resilience to ictogenesis. We explored this hypothesis using *in vitro* electrophysiological characterization of human cortical tissue from epileptogenic and non-epileptogenic areas, which revealed significant differences in DTT (a key determinant of neuronal excitability) variability in the pathological and non-pathological settings. The ability to perform experiments on tissue from human subjects diagnosed with epilepsy makes these results particularly relevant to the human condition. We then implemented these experimentally observed heterogeneities in *in silico* spiking neural networks. Our explorations show that networks with high heterogeneity, similar to the physiological setting, exhibit a more stable asynchronous firing state that is resilient to sudden transitions into a more active and synchronous state. Differing heterogeneity levels also explained the significant differences in the experimentally obtained population activation functions between epileptogenic and non-epileptogenic tissue. Finally, using mathematical analysis, we show that differences in the bifurcation structure of analogous mean-field systems provide a theoretical explanation for dynamical differences in spiking networks. Viewed jointly, these three avenues of investigation provide compelling evidence that reduction in biophysical heterogeneity *exists* in epileptogenic tissue, can *yield dynamical changes* with parallels to seizure onset, and that there are *theoretical principles* underlying these differences.

Computational studies have established the role played by heterogeneity in reducing synchronous activity in the context of physiological gamma rhythms (Börgers and Kopell, 2003, 2005; Börgers et al., 2012). Other investigations have implemented heterogeneity in more varied neural parameters (Yim et al., 2013) and identified asymmetric effects of excitatory and inhibitory heterogeneities on network dynamics (Mejias and Longtin, 2012, 2014). Our study complements and extends the understanding of the role of biophysical heterogeneity in neural networks to human epilepsy by (1) using experimentally derived heterogeneities of the DTT in non-epileptogenic and epileptogenic surgical specimens, which when implemented *in silico* are dynamically relevant; (2) exploring the effects of heterogeneity on the transition to synchrony, a hallmark of seizure onset; and (3) detailing the differing extents to which inhibitory and excitatory heterogeneity contribute to circuit resilience to synchronous transitions. Our mathematical analysis further builds on this work to provide a theoretical undergird for these observed dynamics.

The asymmetric effect of excitatory and inhibitory heterogeneities in our model network supports predictions regarding inhibitory heterogeneity's role in ictogenesis. Figure S3A shows that the sudden onset of synchrony is more likely to arise for moderate values of  $\sigma_i$  than  $\sigma_e$ . The physiological heterogeneity of the entire inhibitory population is likely to be larger than for the excit-

atory population (Cossart, 2011), driven in part by the diverse subpopulations of interneurons (Huang and Paul, 2019). Thus, our work makes two interesting predictions: first, a moderate loss of heterogeneity among inhibitory interneurons might be sufficient to make a system vulnerable to ictogenesis; second, the preservation of inhibitory heterogeneity may provide a bulwark against ictogenesis even if excitatory heterogeneity is pathologically reduced as observed experimentally.

Our modeling suggests that post-synaptic inhibitory heterogeneities, in addition to synaptic mechanisms that underlie the decorrelating function of interneurons (Tetzlaff et al., 2012; Sippy and Yuste, 2013), play an important role in the resilience of circuits to sudden transitions to synchronous states. Thus, in addition to changes in EIB (Dehghani et al., 2016; Žiburkus et al., 2013; Jasper, 2012), it is intriguing to speculate that our results might explain both loss (Cobos et al., 2005; Cossart et al., 2001) and gain of function (Klaassen et al., 2006) alterations in inhibition as reduction in interneuronal homogeneity that reduce resilience to ictogenesis.

It is also interesting to conjecture about how these results might be reconciled with the perspective of epilepsy as a disorder of hyper-excitability and the use of high-frequency oscillations (HFOs) as a marker for the epileptogenic zone. Our findings suggest how interictal hypometabolism observed using positron emission tomography (PET) (Niu et al., 2021) and manifestations of "hyper-excitability," such as inter-ictally recorded HFOs and inter-ictal spikes (IIDs) (Frauscher et al., 2017; Juruska et al., 2017; Zhang et al., 2011; Schevon et al., 2019), may coexist. We propose that the PET hypometabolism may arise in part from cellular homogenization that reduces population excitability (Figures 1C and 5B), since metabolism is tightly linked to firing rate, while this homogenization simultaneously makes the system more vulnerable to transitions into synchronous states (Figure 4C) such as HFOs, IIDs, and seizures.

Notably, previous work has indicated that HFOs arise, in part, from "uninhibited pyramidal cells" (Gulyás and Freund, 2015). Speculatively, this decreased inhibition could arise from a homogenized, and in turn hypo-excitabile, inhibitory population (Figure 5). This may further explain the hypometabolism observed inter-ictally given that interneuronal spiking appears to contribute more to brain metabolism than pyramidal cells (Ackermann et al., 1984). While speculative, the interconnected nature of neural heterogeneity and excitability identified in this work can, at minimum, motivate further studies using targeted patching of interneurons in both human and chronic rodent models to characterize if homogenization occurs in interneuronal populations during epileptogenesis and epilepsy.

Lastly, one might wonder what neurobiological processes render an epileptogenic neuronal population less biophysically diverse. While under physiological conditions channel densities are regulated within neurons to obtain target electrical behaviors (Marder, 2011), it remains speculative as to what processes might lead to pathological homogenization of neuronal populations. However, modeling suggests that biological diversity may be a function of input diversity, so "homogenizing the input received by a population of neurons should lead the population to be less diverse" (Tripathy et al., 2013), possibly through intrinsic plasticity mechanisms (Beck and Yaari, 2008; Zhang

and Linden, 2003). Although requiring further exploration, it is possible that the information-poor, synchronous post-synaptic barrages accompanying a seizure (Trevelyan et al., 2013) represent such a homogenized input, reducing a circuit's resilience to synchronous transitions and promoting epileptogenesis by reducing biophysical heterogeneity.

### Limitations of the study

Our results include fewer neurons from the frontal lobe considering it is a less common source of human cortical tissue than non-epileptogenic MTG. Thus, we use the population of non-epileptogenic frontal lobe neurons only as evidence that heterogeneity levels are not confounded by comparison between the temporal and frontal lobes. The sample size of our epileptogenic neurons was limited by the necessity to confirm the epileptogenicity of the resected cortex using electrocorticography (ECoG), making this dataset highly selective. Although one might obtain a greater sample by comparing non-epileptogenic MTG to epileptogenic mesial temporal structures (i.e., subiculum, parahippocampal gyrus, hippocampus), comparing the allocortex and neocortex would add a further confound. Alternatively, obtaining non-epileptogenic medial temporal lobe cortex is exceedingly rare. With these important limitations in the access to human cortical tissue considered, our comparison between epileptogenic frontal lobe, non-epileptogenic frontal lobe, and non-epileptogenic MTG represent a best-case comparison of the biophysical properties of epileptogenic and non-epileptogenic human tissue while controlling for confounds introduced by the differing brain regions. Our computational and mathematical explorations optimize the conclusions that can be drawn from this rare data.

Our model networks, while analogous to E-I microcircuits commonly used in computational investigations of cortical activity (Renart et al., 2010; Ostojic, 2014; Vogels and Abbott, 2009), are simplified from the biophysical reality and are correspondingly limited. For instance, such models cannot reasonably capture the full richness and complexity of seizure dynamics and do not include multiple inhibitory populations (Huang and Paul, 2019). However, this simplifying choice facilitates findings that have their foundation in fundamental mathematical principles that are not especially reliant on biophysical intricacies such as network topology (see the confirmation of the robustness of our models in Figures S7 and S8).

In addition, experimental limitations arising from patch-clamp experiments limit the number of potential interneurons that can be patched in human tissue, precluding measuring inhibitory DTT and its variability experimentally. Thus, the values of  $\sigma_j$  studied in our model networks were chosen to approximately align with that seen experimentally in the excitatory population while accounting for the possibility of increased inhibitory heterogeneity (Cossart, 2011; Huang and Paul, 2019), with this parameter systematically varied throughout the study.

These limitations warrant the development of biophysically detailed, human-inspired neuron (Rich et al., 2021) and network models (Guet-McCreight et al., 2022; Yao et al., 2022), allowing for the study of additional types of heterogeneity. In this vein, while we do not model seizures per se in this work, the two most common types of seizure onsets observed in intracranial recordings are the low-voltage fast (Lee et al., 2000) and hy-

per-synchronous onsets (Velascol et al., 1999). Both reflect a sudden transition from a desynchronized state to a synchronous oscillation, albeit of differing frequencies. Given the ubiquity of such onsets, our modeling of the transition to synchrony is likely to be broadly relevant to epilepsy.

### STAR★METHODS

Detailed methods are provided in the online version of this paper and include the following:

- KEY RESOURCES TABLE
- RESOURCE AVAILABILITY
  - Lead contact
  - Materials availability
  - Data and code availability
- EXPERIMENTAL MODEL AND SUBJECT DETAILS
- METHOD DETAILS
  - Experiment: Human brain slice preparation
  - Experiment: Electrophysiological recordings and intrinsic physiology feature analysis
  - Modeling: Spiking neural network
  - Modeling: Mean-field reduction
- QUANTIFICATION AND STATISTICAL ANALYSIS

### SUPPLEMENTAL INFORMATION

Supplemental information can be found online at <https://doi.org/10.1016/j.celrep.2022.110863>.

### ACKNOWLEDGMENTS

We thank Frances Skinner, Shreejoy Tripathy, Prajay Shah, and Anukrati Nigam for productive intellectual discussions on this topic in the project's early stages. We thank the National Sciences and Engineering Research Council of Canada (NSERC Grants RGPIN-2017-06662 to J.L. and RGPIN-2015-05936 to T.A.V.), the Krembil Foundation (Krembil Seed Grant to J.L. and T.A.V.), the University of Toronto Department of Physiology (Yuet Ngor Wong Award to S.R.), and the Savoy Foundation (Steriade-Savoy Postdoctoral Fellowship to S.R.) for support of this research.

### AUTHOR CONTRIBUTIONS

Conceptualization: J.L., T.A.V.; methodology: S.R., H.M.C., J.L., T.A.V.; software: S.R., J.L.; validation: S.R., H.M.C.; formal analysis: S.R., H.M.C.; investigation: S.R., H.M.C.; resources: H.M.C., T.A.V.; data curation: S.R., H.M.C.; writing—original draft: S.R.; writing—review and editing: S.R., H.M.C., J.L., T.A.V.; visualization: S.R., H.M.C.; supervision: J.L., T.A.V.; funding acquisition: J.L., T.A.V.

### DECLARATION OF INTERESTS

The authors declare no competing interests.

Received: October 19, 2021

Revised: March 16, 2022

Accepted: May 3, 2022

Published: May 24, 2022, corrected online October 7, 2022

### REFERENCES

Ackermann, R.F., Finch, D.M., Babb, T.L., and Engel, J. (1984). Increased glucose metabolism during long-duration recurrent inhibition of hippocampal

- pyramidal cells. *J. Neurosci.* 4, 251–264. <https://doi.org/10.1523/jneurosci.04-01-00251.1984>.
- Albertson, A.J., Yang, J., and Hablitz, J.J. (2011). Decreased hyperpolarization-activated currents in layer 5 pyramidal neurons enhances excitability in focal cortical dysplasia. *J. Neurophysiol.* 106, 2189–2200. <https://doi.org/10.1152/jn.00164.2011>.
- Altschuler, S.J., and Wu, L.F. (2010). Cellular heterogeneity: do differences make a difference? *Cell* 141, 559–563. <https://doi.org/10.1016/j.cell.2010.04.033>.
- Arnold, E.C., McMurray, C., Gray, R., and Johnston, D. (2019). Epilepsy-induced reduction in hcn channel expression contributes to an increased excitability in dorsal, but not ventral, hippocampal ca1 neurons. *Eneuro* 6. <https://doi.org/10.1523/eneuro.0036-19.2019>.
- Beaulieu-Laroche, L., Toloza, E.H., van der Goes, M.S., Lafourcade, M., Barnagian, D., Williams, Z.M., Eskandar, E.N., Frosch, M.P., Cash, S.S., and Harnett, M.T. (2018). Enhanced dendritic compartmentalization in human cortical neurons. *Cell* 175, 643–651.e14. <https://doi.org/10.1016/j.cell.2018.08.045>.
- Beck, H., and Yaari, Y. (2008). Plasticity of intrinsic neuronal properties in cns disorders. *Nat. Rev. Neurosci.* 9, 357–369. <https://doi.org/10.1038/nrn2371>.
- Berg, J., Sorensen, S.A., Ting, J.T., Miller, J.A., Chartrand, T., Buchin, A., Bakken, T.E., Budzillo, A., Dee, N., Ding, S.L., et al. (2021). Human neocortical expansion involves glutamatergic neuron diversification. *Nature* 598, 151–158. <https://doi.org/10.1038/s41586-021-03813-8>.
- Boland, R.P., Galla, T., and McKane, A.J. (2008). How limit cycles and quasi-cycles are related in systems with intrinsic noise. *J. Stat. Mech. Theor. Exp.* 2008, P09001. <https://doi.org/10.1088/1742-5468/2008/09/p09001>.
- Börger, C., Talei Franzesi, G., LeBeau, F.E.N., Boyden, E.S., and Kopell, N.J. (2012). Minimal size of cell assemblies coordinated by gamma oscillations. *PLoS Comput. Biol.* 8, e1002362. <https://doi.org/10.1371/journal.pcbi.1002362>.
- Börger, C., and Kopell, N. (2003). Synchronization in networks of excitatory and inhibitory neurons with sparse, random connectivity. *Neural Comput.* 15, 509–538. <https://doi.org/10.1162/089976603321192059>.
- Börger, C., and Kopell, N. (2005). Effects of noisy drive on rhythms in networks of excitatory and inhibitory neurons. *Neural Comput.* 17, 557–608. <https://doi.org/10.1162/0899766053019908>.
- Chow, S.N., and Hale, J.K. (2012). *Methods of Bifurcation Theory, volume 251* (Springer Science & Business Media).
- Cobos, I., Calcagnotto, M.E., Vilaythong, A.J., Thwin, M.T., Noebels, J.L., Baraban, S.C., and Rubenstein, J.L.R. (2005). Mice lacking dlx1 show subtype-specific loss of interneurons, reduced inhibition and epilepsy. *Nat. Neurosci.* 8, 1059–1068. <https://doi.org/10.1038/nn1499>.
- Colder, B.W., Frysinger, R.C., Wilson, C.L., Harper, R.M., and Engel, J., Jr. (1996). Decreased neuronal burst discharge near site of seizure onset in epileptic human temporal lobes. *Epilepsia* 37, 113–121. <https://doi.org/10.1111/j.1528-1157.1996.tb00001.x>.
- Cossart, R. (2011). The maturation of cortical interneuron diversity: how multiple developmental journeys shape the emergence of proper network function. *Curr. Opin. Neurobiol.* 21, 160–168. <https://doi.org/10.1016/j.conb.2010.10.003>.
- Cossart, R., Dinocourt, C., Hirsch, J.C., Merchán-Pérez, A., De Felipe, J., Ben-Ari, Y., Esclapez, M., and Bernard, C. (2001). Dendritic but not somatic gabaergic inhibition is decreased in experimental epilepsy. *Nat. Neurosci.* 4, 52–62. <https://doi.org/10.1038/82900>.
- Dehghani, N., Peyrache, A., Telenczuk, B., Le Van Quyen, M., Halgren, E., Cash, S.S., Hatsopoulos, N.G., and Destexhe, A. (2016). Dynamic balance of excitation and inhibition in human and monkey neocortex. *Sci. Rep.* 6, 23176–23212. <https://doi.org/10.1038/srep23176>.
- Frauscher, B., Bartolomei, F., Kobayashi, K., Cimbalnik, J., van 't Klooster, M.A., Ramp, S., Otsubo, H., Höller, Y., Wu, J.Y., Asano, E., Engel, J., Kahane, P., Jacobs, J., and Gotman, J. (2017). High-frequency oscillations: the state of clinical research. *Epilepsia* 58, 1316–1329. <https://doi.org/10.1111/epi.13829>.
- Gluss, B. (1967). A model for neuron firing with exponential decay of potential resulting in diffusion equations for probability density. *Bull. Math. Biophys.* 29, 233–243. <https://doi.org/10.1007/BF02476897>.
- Golder, E.R., and Settle, J.G. (1976). The box-müller method for generating pseudo-random normal deviates. *J. R. Stat. Soc. Ser. C (Applied Statistics)* 25, 12–20. <https://doi.org/10.2307/2346513>.
- Golomb, D., and Rinzel, J. (1993). Dynamics of globally coupled inhibitory neurons with heterogeneity. *Phys. Rev. E* 48, 4810–4814. <https://doi.org/10.1103/physreve.48.4810>.
- Golomb, D., and Rinzel, J. (1994). Clustering in globally coupled inhibitory neurons. *Physica D: Nonlinear Phenomena* 72, 259–282. [https://doi.org/10.1016/0167-2789\(94\)90214-3](https://doi.org/10.1016/0167-2789(94)90214-3).
- Guet-McCreight, A., Moradi Chameh, H., Mahallati, S., Wishart, M., Tripathy, S.J., Valiante, T.A., and Hay, E. (2022). Age-dependent increased sag amplitude in human pyramidal neurons dampens baseline cortical activity. *bioRxiv*.
- Gulyás, A.I., and Freund, T.T. (2015). Generation of physiological and pathological high frequency oscillations: the role of perisomatic inhibition in sharp-wave ripple and interictal spike generation. *Curr. Opin. Neurobiol.* 31, 26–32. <https://doi.org/10.1016/j.conb.2014.07.020>.
- Hodge, R.D., Bakken, T.E., Miller, J.A., Smith, K.A., Barkan, E.R., Graybiel, L.T., Close, J.L., Long, B., Johansen, N., Penn, O., et al. (2019). Conserved cell types with divergent features in human versus mouse cortex. *Nature* 573, 61–68. <https://doi.org/10.1038/s41586-019-1506-7>.
- Huang, Z.J., and Paul, A. (2019). The diversity of gabaergic neurons and neural communication elements. *Nat. Rev. Neurosci.* 20, 563–572. <https://doi.org/10.1038/s41583-019-0195-4>.
- Hutt, A., Lefebvre, J., Hight, D., and Kaiser, H.A. (2020). Phase coherence induced by additive Gaussian and non-Gaussian noise in excitable networks with application to burst suppression-like brain signals. *Front. Appl. Math. Stat.* 5, 69. <https://doi.org/10.3389/fams.2019.00069>.
- Hutt, A., Lefebvre, J., Hight, D., and Sleight, J. (2018). Suppression of underlying neuronal fluctuations mediates EEG slowing during general anaesthesia. *Neuroimage* 179, 414–428. <https://doi.org/10.1016/j.neuroimage.2018.06.043>.
- Hutt, A., Mierau, A., and Lefebvre, J. (2016). Dynamic control of synchronous activity in networks of spiking neurons. *PLoS One* 11, e0161488. <https://doi.org/10.1371/journal.pone.0161488>.
- Jadi, M.P., and Sejnowski, T.J. (2014a). Cortical oscillations arise from contextual interactions that regulate sparse coding. *Proc. Natl. Acad. Sci. U S A* 111, 6780–6785. <https://doi.org/10.1073/pnas.1405300111>.
- Jadi, M.P., and Sejnowski, T.J. (2014b). Regulating cortical oscillations in an inhibition-stabilized network. *Proc. IEEE* 102, 830–842. <https://doi.org/10.1109/jproc.2014.2313113>.
- Jasper, H.H. (2012). *Jasper's Basic Mechanisms of the Epilepsies, volume 80* (OUP USA).
- Jirsa, V.K., Stacey, W.C., Quilichini, P.P., Ivanov, A.I., and Bernard, C. (2014). On the nature of seizure dynamics. *Brain* 137, 2210–2230. <https://doi.org/10.1093/brain/awu133>.
- Jiruska, P., Alvarado-Rojas, C., Schevon, C.A., Staba, R., Stacey, W., Wendling, F., and Avoli, M. (2017). Update on the mechanisms and roles of high-frequency oscillations in seizures and epileptic disorders. *Epilepsia* 58, 1330–1339. <https://doi.org/10.1111/epi.13830>.
- Jiruska, P., De Curtis, M., Jefferys, J.G.R., Schevon, C.A., Schiff, S.J., and Schindler, K. (2013). Synchronization and desynchronization in epilepsy: controversies and hypotheses. *J. Physiol.* 591, 787–797. <https://doi.org/10.1113/jphysiol.2012.239590>.
- Kalmbach, B.E., Buchin, A., Long, B., Close, J., Nandi, A., Miller, J.A., Bakken, T.E., Hodge, R.D., Chong, P., de Frates, R., et al. (2018). h-channels contribute to divergent intrinsic membrane properties of supragranular pyramidal neurons in human versus mouse cerebral cortex. *Neuron* 100, 1194–1208.e5. <https://doi.org/10.1016/j.neuron.2018.10.012>.
- Kalmbach, B.E., Hodge, R.D., Jorstad, N.L., Owen, S., de Frates, R., Yanny, A.M., Dalley, R., Mallory, M., Graybiel, L.T., Radaelli, C., et al. (2021). Signature morpho-electric, transcriptomic, and dendritic properties of human layer 5

- neocortical pyramidal neurons. *Neuron* 109, 2914–2927.e5. <https://doi.org/10.1016/j.neuron.2021.08.030>.
- Klaassen, A., Glykys, J., Maguire, J., Labarca, C., Mody, I., and Boulter, J. (2006). Seizures and enhanced cortical gabaergic inhibition in two mouse models of human autosomal dominant nocturnal frontal lobe epilepsy. *Proc. Natl. Acad. Sci. U S A* 103, 19152–19157. <https://doi.org/10.1073/pnas.0608215103>.
- Kramer, M.A., Kirsch, H.E., and Szeri, A.J. (2005). Pathological pattern formation and cortical propagation of epileptic seizures. *J. R. Soc. Interf.* 2, 113–127. <https://doi.org/10.1098/rsif.2004.0028>.
- Krishnamoorthy, K., and Lee, M. (2014). Improved tests for the equality of normal coefficients of variation. *Comput. Stat.* 29, 215–232. <https://doi.org/10.1007/s00180-013-0445-2>.
- Lee, S.A., Spencer, D.D., and Spencer, S.S. (2000). Intracranial eeg seizure-onset patterns in neocortical epilepsy. *Epilepsia* 41, 297–307. <https://doi.org/10.1111/j.1528-1157.2000.tb00159.x>.
- Lefebvre, J., Hutt, A., Knebel, J.F., Whittingstall, K., and Murray, M.M. (2015). Stimulus statistics shape oscillations in nonlinear recurrent neural networks. *J. Neurosci.* 35, 2895–2903. <https://doi.org/10.1523/jneurosci.3609-14.2015>.
- Marder, E. (2011). Variability, compensation, and modulation in neurons and circuits. *Proc. Natl. Acad. Sci. U S A* 108, 15542–15548. <https://doi.org/10.1073/pnas.1010674108>.
- Marder, E., and Goaillard, J.M. (2006). Variability, compensation and homeostasis in neuron and network function. *Nat. Rev. Neurosci.* 7, 563–574. <https://doi.org/10.1038/nrn1949>.
- Marwick, B., and Krishnamoorthy, K. (2019). cvequality: tests for the equality of coefficients of variation from multiple groups. <https://github.com/benmarwick/cvequality>. R package version 0.1.3.
- MATLAB (2019). version 9.6.0 (R2019a) (The MathWorks Inc.).
- Mejias, J.F., and Longtin, A. (2012). Optimal heterogeneity for coding in spiking neural networks. *Phys. Rev. Lett.* 108, 228102. <https://doi.org/10.1103/physrevlett.108.228102>.
- Mejias, J.F., and Longtin, A. (2014). Differential effects of excitatory and inhibitory heterogeneity on the gain and asynchronous state of sparse cortical networks. *Front. Comput. Neurosci.* 8, 107. <https://doi.org/10.3389/fncom.2014.00107>.
- Mishra, P., and Narayanan, R. (2019). Disparate forms of heterogeneities and interactions among them drive channel decorrelation in the dentate gyrus: degeneracy and dominance. *Hippocampus* 29, 378–403. <https://doi.org/10.1002/hipo.23035>.
- Moradi Chameh, H., Rich, S., Wang, L., Chen, F.D., Zhang, L., Carlen, P.L., Tripathy, S.J., and Valiante, T.A. (2021). Diversity amongst human cortical pyramidal neurons revealed via their sag currents and frequency preferences. *Nat. Commun.* 12, 2497. <https://doi.org/10.1038/s41467-021-22741-9>.
- Neske, G.T., Patrick, S.L., and Connors, B.W. (2015). Contributions of diverse excitatory and inhibitory neurons to recurrent network activity in cerebral cortex. *J. Neurosci.* 35, 1089–1105. <https://doi.org/10.1523/jneurosci.2279-14.2015>.
- Niu, N., Xing, H., Wu, M., Ma, Y., Liu, Y., Ba, J., Zhu, S., Li, F., and Huo, L. (2021). Performance of pet imaging for the localization of epileptogenic zone in patients with epilepsy: a meta-analysis. *Eur. Radiol.* 31, 6353–6366. <https://doi.org/10.1007/s00330-020-07645-4>.
- Ostojic, S. (2014). Two types of asynchronous activity in networks of excitatory and inhibitory spiking neurons. *Nat. Neurosci.* 17, 594–600. <https://doi.org/10.1038/nn.3658>.
- Padmanabhan, K., and Urban, N.N. (2010). Intrinsic biophysical diversity decorrelates neuronal firing while increasing information content. *Nat. Neurosci.* 13, 1276–1282. <https://doi.org/10.1038/nn.2630>.
- Planert, H., Mittermaier, F.X., Gresser, S., Fidzinski, P., Schneider, U.C., Radbruch, H., Onken, J., Holtkamp, M., Schmitz, D., Alle, H., et al. (2021). Intra-individual physiomic landscape of pyramidal neurons in the human neocortex. Preprint at bioRxiv. <https://doi.org/10.1101/2021.11.08.467668>.
- Renart, A., De La Rocha, J., Bartho, P., Hollender, L., Parga, N., Reyes, A., and Harris, K.D. (2010). The asynchronous state in cortical circuits. *Science* 327, 587–590. <https://doi.org/10.1126/science.1179850>.
- Reynolds, E.H. (2002). Introduction: epilepsy in the world. *Epilepsia* 43, 1–3. <https://doi.org/10.1046/j.1528-1157.43.s.6.1.x>.
- Rich, S., Booth, V., and Zochowski, M. (2016). Intrinsic cellular properties and connectivity density determine variable clustering patterns in randomly connected inhibitory neural networks. *Front. Neural Circuits* 10, 82. <https://doi.org/10.3389/fncir.2016.00082>.
- Rich, S., Chameh, H.M., Rafiee, M., Ferguson, K.A., Skinner, F.K., Valiante, T.A., and Valiente, T.A. (2020a). Inhibitory network bistability explains increased interneuronal activity prior to seizure onset. *Front. Neural Circuits* 13, 81. <https://doi.org/10.3389/fncir.2019.00081>.
- Rich, S., Hutt, A., Skinner, F.K., Valiante, T.A., and Lefebvre, J. (2020b). Neurostimulation stabilizes spiking neural networks by disrupting seizure-like oscillatory transitions. *Scientific Rep.* 10, 15408–15417. <https://doi.org/10.1038/s41598-020-72335-6>.
- Rich, S., Moradi Chameh, H., Sekulic, V., Valiante, T.A., and Skinner, F.K. (2021). Modeling reveals human–rodent differences in h-current kinetics influencing resonance in cortical layer 5 neurons. *Cereb. Cortex* 31, 845–872. <https://doi.org/10.1093/cercor/bhaa261>.
- Rich, S., Zochowski, M., and Booth, V. (2017). Dichotomous dynamics in ei networks with strongly and weakly intra-connected inhibitory neurons. *Front. Neural Circuits* 11, 104. <https://doi.org/10.3389/fncir.2017.00104>.
- Rich, S., Zochowski, M., and Booth, V. (2018). Effects of neuromodulation on excitatory–inhibitory neural network dynamics depend on network connectivity structure. *J. Nonlinear Sci.* 30, 2171–2194. <https://doi.org/10.1007/s00332-017-9438-6>.
- Saggio, M.L., Crisp, D., Scott, J.M., Karoly, P., Kuhlmann, L., Nakatani, M., Murai, T., Dumpelmann, M., Schulze-Bonhage, A., Ikeda, A., et al. (2020). A taxonomy of seizure dynamotypes. *Elife* 9, e55632. <https://doi.org/10.7554/elif55632>.
- Savov, V.N., and Todorov, G. (2000). On a method for determining limit cycles in nonlinear circuits. *Int. J. Electronics* 87, 827–840. <https://doi.org/10.1080/00207210050028760>.
- Schevon, C.A., Tobochnik, S., Eissa, T., Merricks, E., Gill, B., Parrish, R.R., Bateman, L.M., McKhann, G.M., Jr., Emerson, R.G., and Trevelyan, A.J. (2019). Multiscale recordings reveal the dynamic spatial structure of human seizures. *Neurobiol. Dis.* 127, 303–311. <https://doi.org/10.1016/j.nbd.2019.03.015>.
- Schwartzkroin, P.A., Turner, D.A., Knowles, W.D., and Wyler, A.R. (1983). Studies of human and monkey “epileptic” neocortex in the in vitro slice preparation. *Ann. Neurol. Official J. Am. Neurol. Assoc. Child Neurol. Soc.* 13, 249–257. <https://doi.org/10.1002/ana.410130305>.
- Sippy, T., and Yuste, R. (2013). Decorrelating action of inhibition in neocortical networks. *J. Neurosci.* 33, 9813–9830. <https://doi.org/10.1523/jneurosci.4579-12.2013>.
- Snyder, D.L., and Miller, M.I. (2012). *Random Point Processes in Time and Space* (Springer Science & Business Media).
- Stefanescu, R.A., Shivakeshavan, R.G., and Talathi, S.S. (2012). Computational models of epilepsy. *Seizure* 21, 748–759. <https://doi.org/10.1016/j.seizure.2012.08.012>.
- Stevens, C.F., and Zador, A.M. (1996). When is an integrate-and-fire neuron like a Poisson neuron? In *Advances in Neural Information Processing Systems*, pp. 103–109.
- Sutula, T.P., and Dudek, F.E. (2007). Unmasking recurrent excitation generated by mossy fiber sprouting in the epileptic dentate gyrus: an emergent property of a complex system. *Prog. Brain Res.* 163, 541–563. [https://doi.org/10.1016/s0079-6123\(07\)63029-5](https://doi.org/10.1016/s0079-6123(07)63029-5).
- Testa-Silva, G., Verhoog, M.B., Linaro, D., de Kock, C.P.J., Baayen, J.C., Meredith, R.M., De Zeeuw, C.I., Giugliano, M., and Mansvelde, H.D. (2014). High bandwidth synaptic communication and frequency tracking in human neocortex. *PLoS Biol.* 12, e1002007. <https://doi.org/10.1371/journal.pbio.1002007>.

- Tetzlaff, T., Helias, M., Einevoll, G.T., and Diesmann, M. (2012). Decorrelation of neural-network activity by inhibitory feedback. *PLoS Comput. Biol.* 8, e1002596. <https://doi.org/10.1371/journal.pcbi.1002596>.
- Traub, R.D., Jefferys, J.G., and Whittington, M.A. (1997). Simulation of gamma rhythms in networks of interneurons and pyramidal cells. *J. Comput. Neurosci.* 4, 141–150. <https://doi.org/10.1023/a:1008839312043>.
- Trevelyan, A.J., Bruns, W., Mann, E.O., Crepel, V., and Scanziani, M. (2013). The information content of physiological and epileptic brain activity. *J. Physiol.* 591, 799–805. <https://doi.org/10.1113/jphysiol.2012.240358>.
- Tripathy, S.J., Padmanabhan, K., Gerkin, R.C., and Urban, N.N. (2013). Intermediate intrinsic diversity enhances neural population coding. *Proc. Natl. Acad. Sci. U S A* 110, 8248–8253. <https://doi.org/10.1073/pnas.1221214110>.
- Valiante, T. (2009). Selective Amygdalohippocampectomy. In *Textbook of Stereotactic and Functional Neurosurgery*, 2nd, A.M. Lozano, P.L. Gildenberg, and R. Tasker, eds. (Springer), pp. 2677–2714.
- Velascol, A.L., Wilson, C.L., Babb, T.L., and Engel Jr, J. (1999). Functional and anatomic correlates of two frequently observed temporal lobe seizure-onset patterns. *Neural Plasticity* 7, 49–63. <https://doi.org/10.1155/np.2000.49>.
- Vogels, T.P., and Abbott, L.F. (2009). Gating multiple signals through detailed balance of excitation and inhibition in spiking networks. *Nat. Neurosci.* 12, 483–491. <https://doi.org/10.1038/nn.2276>.
- Yao, H.K., Guet-McCreight, A., Mazza, F., Moradi Chameh, H., Prevot, T.D., Griffiths, J.D., Tripathy, S.J., Valiante, T.A., Sibille, E., and Hay, E. (2022). Reduced inhibition in depression impairs stimulus processing in human cortical microcircuits. *Cell Reports* 38. <https://doi.org/10.1016/j.celrep.2021.110232>.
- Yim, M.Y., Aertsen, A., and Rotter, S. (2013). Impact of intrinsic biophysical diversity on the activity of spiking neurons. *Phys. Rev. E* 87, 032710. <https://doi.org/10.1103/physreve.87.032710>.
- Zhang, W., and Linden, D.J. (2003). The other side of the engram: experience-driven changes in neuronal intrinsic excitability. *Nat. Rev. Neurosci.* 4, 885–900. <https://doi.org/10.1038/nrn1248>.
- Zhang, Z., Valiante, T., and Carlen, P. (2011). Transition to seizure: from “macro”-to “micro”-mysteries. *Epilepsy Res.* 97, 290–299. <https://doi.org/10.1016/j.eplepsyres.2011.09.025>.
- Žiburkus, J., Cressman, J.R., and Schiff, S.J. (2013). Seizures as imbalanced up states: excitatory and inhibitory conductances during seizure-like events. *J. Neurophysiol.* 109, 1296–1306. <https://doi.org/10.1152/jn.00232.2012>.

## STAR★METHODS

### KEY RESOURCES TABLE

| REAGENT or RESOURCE  | SOURCE  | IDENTIFIER  |
|--|---|---|
| <b>Biological samples</b>  |   |   |
| Cortical Human tissues   | Toronto Western Hospital                                    | N/A   |
| <b>Chemicals, peptides, and recombinant proteins</b>                     |   |   |
| Sucrose  | Bioshop Canada  | CAS#57-50-1   |
| MgSO <sub>4</sub> ·7H <sub>2</sub> O                                     | Fisher reagents   | CAS#10034-99-8  |
| CaCl <sub>2</sub> ·2H <sub>2</sub> O                                     | Fisher reagents   | CAS#10035-04-8  |
| NaHCO <sub>3</sub>   | Bioshop Canada  | CAS#144-55-8  |
| NaH <sub>2</sub> PO <sub>4</sub> ·H <sub>2</sub> O                       | Fisher reagents   | CAS#10049-21-5  |
| KCl  | Fisher reagents   | CAS#7447-40-7   |
| D-glucose  | Sigma   | CAS#50-99-7   |
| K-Gluconate  | Sigma   | CAS#299-27-4  |
| NaCl   | Bioshop Canada  | CAS#7647-14-5   |
| HEPES  | Bioshop Canada  | CAS#7365-45-9   |
| MgCl <sub>2</sub>  | Bioshop Canada  | CAS#7791-18-6   |
| Na <sub>2</sub> ATP  | Sigma   | CAS#34369-07-8  |
| GTP  | Sigma   | CAS#36051-31-7  |
| <b>Deposited data</b>  |   |   |
| Patch clamp recordings from human cortical layer 5 pyramidal neurons     | This paper and <a href="#">Moradi Chameh et al., (2021)</a> | <a href="https://doi.org/10.5281/zenodo.6458364">https://doi.org/10.5281/zenodo.6458364</a>                 |
| <b>Experimental models: Organisms/strains</b>                            |   |   |
| Cortical Human tissues   | Toronto Western Hospital                                    | N/A   |
| <b>Software and algorithms</b>   |   |   |
| MATLAB R2019A  | MathWorks   | <a href="https://www.mathworks.com/products/matlab.html">https://www.mathworks.com/products/matlab.html</a> |
| Spiking and mean-field cortical E-I neural microcircuits, coded in C/C++ | This paper  | <a href="https://doi.org/10.5281/zenodo.6458364">https://doi.org/10.5281/zenodo.6458364</a>                 |
| GraphPad Prism 6   | GraphPad Software   | <a href="https://www.graphpad.com/">https://www.graphpad.com/</a>   |
| Clampfit10.7   | Molecular devices   | <a href="https://support.moleculardevices.com">https://support.moleculardevices.com</a>                     |
| Python   | Python Software Foundation                                  | <a href="https://www.python.org/">https://www.python.org/</a>   |
| R software   | R Software Foundation                                       | <a href="http://www.r-project.org">www.r-project.org</a>  |

### RESOURCE AVAILABILITY

#### Lead contact

Further information and requests for resources and code should be directed to and will be fulfilled by the lead contact, Scott Rich ([scott.rich@uhnresearch.ca](mailto:scott.rich@uhnresearch.ca)).

#### Materials availability

This study did not generate new unique reagents.

#### Data and code availability

- Experimental data as reported in [Figure 1](#) and [Figure S1](#) have been deposited at <https://github.com/Valiantelab/LostNeuralHeterogeneity> and via Zenodo, and are publicly available as of the date of publication. The DOI is listed in the [key resources table](#). The simulation data and the raw experimental data are available upon request to the [lead contact](#).
- All original code is openly accessible at <https://github.com/Valiantelab/LostNeuralHeterogeneity> and via Zenodo at <https://doi.org/10.5281/zenodo.6470912> as of the date of publication. DOIs are listed in the [key resources table](#).

- Any additional information required to reanalyze the data reported in this work is available from the [lead contact](#) upon request.

## EXPERIMENTAL MODEL AND SUBJECT DETAILS

All procedures on human tissue were performed in accordance with the Declaration of Helsinki and approved by the University Health Network Research Ethics board. Patients underwent a standardized temporal or frontal lobectomy under general anesthesia using volatile anesthetics for seizure treatment (Valiante, 2009). Tissue was obtained from patients diagnosed with temporal or frontal lobe epilepsy, or patients undergoing tumor resection, who provided written consent. Demographic information (including age, sex, and diagnosis) was obtained and anonymized as stated in the research protocol, although full demographic information was not available for every patient.

Tissue from temporal lobe was obtained from 22 patients, 12 male and 8 female (2 sex unknown), age ranging between 21 and 63 years (mean age  $\pm$  SEM:  $37.8 \pm 2.9$ ), with 1-9 cells studied per patient. The resected temporal lobe tissue displayed no structural or functional abnormalities in preoperative MRI and was deemed “healthy” tissue considering it is located outside of the epileptogenic zone. Tissue from epileptogenic frontal lobe was obtained from five patients, 4 female and 1 male, age ranging between 23 and 36 years (mean age  $\pm$  SEM:  $30.2 \pm 2.4$ ), and was deemed “epileptogenic” tissue as confirmed using electrocorticography (ECoG), making this data set highly selective. 1-5 cells were studied per patient. Tissue from non-epileptogenic frontal lobe obtained during tumor resection was obtained from two patients, both female, ages 37 and 58 years, with 8 and 4 cells studied per patient, and was also considered “healthy, non-epileptogenic” tissue as it was taken away from the tumor itself. This tissue is a common source of human cortical tissue to study human cell and circuit properties (Kalmbach et al., 2018, 2021; Testa-Silva et al., 2014).

## METHOD DETAILS

### Experiment: Human brain slice preparation

After surgical resection, the cortical tissue block was instantaneously submerged in ice-cold ( $\sim 4^{\circ}\text{C}$ ) cutting solution that was continuously bubbled with 95%  $\text{O}_2$ -5%  $\text{CO}_2$  containing (in mM): sucrose 248, KCl 2,  $\text{MgSO}_4 \cdot 7\text{H}_2\text{O}$  0.3,  $\text{CaCl}_2 \cdot 2\text{H}_2\text{O}$  1,  $\text{NaHCO}_3$  26,  $\text{NaH}_2\text{PO}_4 \cdot \text{H}_2\text{O}$  1.25, and D-glucose 10. The osmolarity was adjusted to 300-305 mOsm. The human tissue samples were transported (5-10 min) from Toronto Western Hospital (TWH) to the laboratory for further slice processing. Transverse brain slices (400  $\mu\text{m}$ ) were obtained using a vibratome (Leica 1200 V) perpendicular to the pial surface to ensure that pyramidal cell dendrites were minimally truncated (Beaulieu-Laroche et al., 2018; Kalmbach et al., 2018) in the same cutting solution as used for transport. The total duration, including slicing and transportation, was kept to a maximum of 20-30 min. After sectioning, the slices were incubated for 30 min at  $34^{\circ}\text{C}$  in standard artificial cerebrospinal fluid (aCSF) (in mM): NaCl 123, KCl 4,  $\text{CaCl}_2 \cdot 2\text{H}_2\text{O}$  1,  $\text{MgSO}_4 \cdot 7\text{H}_2\text{O}$  1,  $\text{NaHCO}_3$  26,  $\text{NaH}_2\text{PO}_4 \cdot \text{H}_2\text{O}$  1.2, and D-glucose 10. The pH was 7.40 and after incubation the slice was held for at least for 60 min at room temperature. aCSF in both incubation and recording chambers were continuously bubbled with carbogen gas (95%  $\text{O}_2$ -5%  $\text{CO}_2$ ) and had an osmolarity of 300-305 mOsm.

### Experiment: Electrophysiological recordings and intrinsic physiology feature analysis

Slices were transferred to a recording chamber mounted on a fixed-stage upright microscope (Axioskop 2 FS MOT; Carl Zeiss, Germany). Recordings were performed from the soma of pyramidal neurons at  $32$ - $34^{\circ}$  in recording aCSF continually perfused at 4 mL/min. Cortical neurons were visualized using an IR-CCD camera (IR-1000, MTI, USA) with a  $40\times$  water immersion objective lens. Using the IR-DIC microscope, the boundary between layer 1 (L1) and 2 (L2) was easily distinguishable in terms of cell density. Below L2, the sparser area of neurons (L3) was followed by a tight band of densely packed layer 4 (L4) neurons, with a decrease in cell density indicating layer 5 (L5) (Moradi Chameh et al., 2021; Kalmbach et al., 2021).

Patch pipettes (3-6 M  $\Omega$  resistance) were pulled from standard borosilicate glass pipettes (thin-wall borosilicate tubes with filaments, World Precision Instruments, Sarasota, FL, USA) using a vertical puller (PC-10, Narishige). Pipettes were filled with intracellular solution containing (in mM): K-gluconate 135; NaCl 10; HEPES 10;  $\text{MgCl}_2$  1;  $\text{Na}_2\text{ATP}$  2; GTP 0.3, pH adjusted with KOH to 7.4 (290-309 mOsm).

Whole-cell patch-clamp recordings were obtained using a Multiclamp 700A amplifier, Axopatch 200B amplifier, pClamp 9.2 and pClamp 10.6 data acquisition software (Axon instruments, Molecular Devices, USA). Electrical signals were digitized at 20 kHz using a 1320X digitizer. The access resistance was monitored throughout the recording (typically between 8 and 25 M  $\Omega$ ), and neurons were discarded if the access resistance was  $> 25$  M  $\Omega$ . The liquid junction potential was calculated to be  $-10.8$  mV and was not corrected.

Electrophysiological data were analyzed off-line using Clampfit 10.7, Python and MATLAB (MATLAB, 2019). Electrophysiological features were calculated from responses elicited by 600 ms square current steps as previously described (Moradi Chameh et al., 2021). Briefly, the resting membrane potential (RMP) was measured after breaking into the cell ( $\text{IC} = 0$ ). The firing threshold was determined following depolarizing current injections between 50 and 250 pA with 50 pA step size for 600 ms; the threshold was calculated by finding the voltage value corresponding with a value of  $\frac{dV}{dt}$  that was 5% of the average maximal  $\frac{dV}{dt}$  across all action potentials elicited by the input current that first yielded action potential firing. The distance to threshold presented in this paper was calculated as the difference between the RMP and threshold. The average FI curve (i.e., activation function) was generated by calculating the



instantaneous frequency at each spike for each of the depolarizing current injections (50-250 pA, step size 50 pA, 600 ms) and averaging over the population. Spike frequency adaptation ratio was calculated from the first current injection that yielded at least four spikes, and is defined as the mean of the ratio of subsequent inter-spike intervals. This could not be quantified in every neuron if sufficient spiking was not elicited by the current-clamp protocol. This analysis utilizes the IPFX package made available through the Allen Institute (<https://github.com/AllenInstitute/ipfx>), as used by Berg et al. (2021) amongst others.

### Modeling: Spiking neural network

The cortical spiking neural network contains populations of recurrently connected excitatory and inhibitory neurons (Snyder and Miller, 2012; Stevens and Zador, 1996). The spiking response of those neurons obeys the non-homogeneous Poisson process

$$Y^j \rightarrow \text{Poisson}(f(u_x^j, h^j)) \quad (\text{Equation 1})$$

where  $Y^j = \sum_k \delta(t - t_k)$  is a Poisson spike train with rate  $f(u_x^j, h^j)$ .

The firing rate of neuron  $j$  is determined by the non-linear sigmoidal activation function  $f(u_x^j, h^j)$ ,

$$f(u_x^j, h^j) = \frac{1}{1 + e^{-\beta(u_x^j - h^j)}} \quad (\text{Equation 2})$$

where  $u_x^j$  is the membrane potential analogue ( $x = e$  whenever  $j$  is an excitatory neuron, and  $x = i$  whenever  $j$  is an inhibitory neuron) and  $h^j$  represents the rheobase. The constant  $\beta = 4.8$  scales the non-linear gain.

Heterogeneity is implemented via the rheobases  $h^j$ . The  $h^j$  values are chosen by independently and randomly sampling a normal Gaussian distribution whose standard deviation is  $\sigma_{e,i}$  if neuron  $j$  is excitatory ( $e$ ) or inhibitory ( $i$ ). The values of  $\sigma_i$  and  $\sigma_e$  are varied throughout these explorations between a minimum value of 2.5 mV and a maximum value of 16.75 mV. The heterogeneity parameters for the model have a direct parallel with the heterogeneity in the distance to threshold (DTT) measured experimentally, with  $\beta$  chosen so that the experimentally observed heterogeneity values and the heterogeneity parameters implemented in the model are within the same range (compare Figures 1B, 2C, and 2D).

The membrane potential analogue  $u_x^j$  obeys the following dynamics:

$$\alpha_x^{-1} \frac{du_x^j}{dt} = (-u_x^j(t) + \text{Syn}_{ex}^j + \text{Syn}_{ix}^j + I_x^o + I_x(t)) + \sqrt{2D} \chi_x^j \quad (\text{Equation 3})$$

The variable  $\alpha_x$  represents the rate constant depending upon whether the neuron  $j$  is excitatory ( $x = e$ ,  $\alpha_e = 100$  Hz) or inhibitory ( $x = i$ ,  $\alpha_i = 200$  Hz). The differential time scales are implemented given the different membrane time constants between cortical pyramidal neurons and parvalbumin positive (PV) interneurons (Neske et al., 2015).

$\text{Syn}_{ex}^j$  and  $\text{Syn}_{ix}^j$  are the synaptic inputs to the cell  $j$  (from the excitatory and inhibitory populations, respectively), dependent upon whether cell  $j$  is excitatory ( $x = e$ ) or inhibitory ( $x = i$ ). Our cortical model is built of 800 excitatory ( $N_e$ ) and 200 inhibitory neurons ( $N_i$ ) (Traub et al., 1997; Rich et al., 2017, 2018). The connectivity density for each connection type (E-E, E-I, I-E, and I-I) is varied uniformly via a parameter  $p$ . In this study,  $p = 1$  is used (i.e., all-to-all connectivity) with the exception of in Figure S6. The synaptic strengths are represented by  $w_{xy}$  where  $x, y = e, i$  depending upon whether the pre-synaptic cell ( $x$ ) and the post-synaptic cell ( $y$ ) are excitatory or inhibitory. In our model,  $w_{ee} = 100.000$ ,  $w_{ei} = 187.500$ ,  $w_{ie} = -293.750$ , and  $w_{ii} = -8.125$ . Negative signs represent inhibitory signaling, while positive signs represent excitatory signalling. These values are chosen to place the network near a tipping point between asynchronous and synchronous firing based on mathematical analysis and previous modeling work (Rich et al., 2020b), and scaled relative to the values of  $\beta$ .

The post-synaptic inputs  $\text{Syn}_{ex}^j$  and  $\text{Syn}_{ix}^j$  are given by

$$\text{Syn}_{ex}^j = \frac{1}{N_e} \sum_{k=1, k \neq j}^{N_e} c^{kj} \frac{w_{ex}}{p} Y^k(t - \Delta t) \quad (\text{Equation 4})$$

$$\text{Syn}_{ix}^j = \frac{1}{N_i} \sum_{k=1, k \neq j}^{N_i} c^{kj} \frac{w_{ix}}{p} Y^k(t - \Delta t) \quad (\text{Equation 5})$$

where  $x = e, i$  and  $Y^k$  is a Poisson spike train given by  $Y^k = \sum_l \delta(t - t_l)$ . The connectivity scheme excludes self-synapses.  $c^{kj}$  represents the connectivity: if neuron  $k$  synapses onto neuron  $j$ ,  $c^{kj} = 1$ , and otherwise  $c^{kj} = 0$ . The synaptic weights are scaled by the connectivity density  $p$  so that the net input signal to each neuron is not affected by the number of connections.

Equation 3 includes three non-synaptic inputs to the neuron:  $I_x^o$ ,  $I_x(t)$ , and  $\sqrt{2D} \chi_x^j$ . The variable  $\chi_x^j$  is a spatially independent Gaussian white noise process. The value of noise intensity was chosen so that the noise-induced fluctuations are commensurate with endogenous dynamics of the network.  $I_x^o$  represents a bias current whose value depends on whether the neuron is excitatory

( $x = e$ ) or inhibitory ( $x = i$ ), imparting a differential baseline spiking rate to these distinct populations. Here,  $I_i^p = -31.250$ , ensuring that inhibitory neurons will typically require excitatory input to fire.  $I_e^p = -15.625$  is based on previous literature (Jadi and Sejnowski, 2014a, b; Neske et al., 2015; Rich et al., 2020b) to position the system near the transition between asynchronous and synchronous firing.

$I_x(t)$  implements time-varying external input only applied to the excitatory population (this is simply referred to as the “drive” to the system in Figures 2, 3, and 4).  $I_i(t) = 0$  for inhibitory neurons. In this work, this term is used primarily to study the response of the spiking network to a linear ramp excitatory input that occurs at a time scale much slower than the dynamics of individual neurons: to yield the ramp current used throughout the study  $I_e(t)$  simply varies linearly between 0 and 31.25 over a 2500 ms simulation (for computational efficiency, the simulation length is limited to 2048 ms for the heatmaps displayed in Figures S3 and S6). In Figure S3B, where we characterize the dynamics of the network with constant input,  $I_e(t) = 15.625$  uniformly.

The final probability of a Poisson neuron  $j$  firing at time  $t$  depends upon the effect of these various elements on  $u_x^j$ :

$$\rho^j = 1 - e^{-f(u_x^j(t), h^j) dt} \quad (\text{Equation 6})$$

### Parameter values

Parameter values, summarized in the table of key model parameters below, are analogous to those used in previous work on oscillatory cortical networks (Jadi and Sejnowski, 2014a, b; Neske et al., 2015; Rich et al., 2020b) with the scaling of our chosen  $\beta$  accounted for.

Key model parameters.

| Parameter   | Value    |
|---|----------|
| Number of excitatory neurons, $N_e$               | 800      |
| Number of inhibitory neurons, $N_i$               | 200      |
| Excitatory rate constant, $\alpha_e$              | 100 Hz   |
| Inhibitory rate constant, $\alpha_i$              | 200 Hz   |
| Non-linear gain of activation function, $\beta$   | 4.8      |
| Variance of noisy input, $D$                      | 3.906    |
| Excitatory bias current, $I_e^p$                  | -15.625  |
| Inhibitory bias current, $I_i^p$                  | -31.250  |
| External input, $I_e(t)$                          | Variable |
| Excitatory-excitatory synaptic strength, $w_{ee}$ | 100.000  |
| Excitatory-inhibitory synaptic strength, $w_{ei}$ | 187.500  |
| Inhibitory-inhibitory synaptic strength, $w_{ii}$ | -8.125   |
| Inhibitory-excitatory synaptic strength, $w_{ie}$ | -293.750 |
| Excitatory heterogeneity, $\sigma_e$              | Variable |
| Inhibitory heterogeneity, $\sigma_i$              | Variable |
| rheobase, $h^j$                                   | Variable |
| Connectivity density, $\rho$                      | Variable |
| Time step, $\Delta t$                             | 1 ms     |

### Numerics

All sampling from standard normal Gaussian distributions is done via the Box-Mueller algorithm (Golder and Settle, 1976). Equations are integrated using the Euler-Maruyama method. In our simulations,  $\Delta t = 0.1$ , scaled so that each time step  $\Delta t$  represents 1 ms.

The excitatory network synchrony (i.e. Synchrony Measure) and excitatory and inhibitory firing rates are calculated over sliding 100 ms time windows in Figures 2, 3, and 4. To preserve symmetry and ensure initial transients do not skew the data, our first window begins at  $t = 100$ .

The Synchrony Measure is an adaptation of a commonly used measure developed by Golomb and Rinzel (Golomb and Rinzel, 1993, 1994) to quantify the degree of coincident spiking in a network as utilized in our previous studies (Rich et al., 2016, 2017, 2018; 2020a). We apply this measure in this work exclusively to the population of excitatory cells. Briefly, the measure involves convolving a very narrow Gaussian function with the time of each action potential for every cell to generate functions  $V^i(t)$ . The population averaged voltage  $V(t)$  is then defined as  $V(t) = \frac{1}{N_e} \sum_{i=1}^{N_e} V^i(t)$ , where  $N$  is the number of cells in the network. The overall variance of the population averaged voltage  $\text{Var}(V)$  and the variance of an individual neuron’s voltage  $\text{Var}(V^i)$  is defined as

$$\text{Var}(V) = \langle V(t)^2 \rangle - \langle V(t) \rangle^2 \quad (\text{Equation 7})$$

and

$$\text{Var}(V^i) = \langle V^i(t)^2 \rangle - \langle V^i(t) \rangle^2 \quad (\text{Equation 8})$$

where  $\langle \cdot \rangle$  indicates time averaging over the interval for which the measure is taken. The Synchrony Measure  $S$  is then defined as

$$S = \frac{\text{Var}(V)}{\frac{1}{N_e} \sum_{i=1}^{N_e} \text{Var}(V^i)} \quad (\text{Equation 9})$$

The value  $S = 0$  indicates completely asynchronous firing, while  $S = 1$  corresponds to fully synchronous network activity. Intermediate values represent intermediate degrees of synchronous firing.

In the case of sliding time bins, this measure is taken by only considering spikes falling into the time window of interest. In [Figure 4](#) we present averages of  $S$  over 100 independent realizations, and if a particular run yields a “NaN” result for  $S$  at a given time step (indicating no spikes in the associated window), we eliminate that value from the average for that time point (this increases the variability of these values since there are less to average over; thus, this is reflected in an increased range of the  $\pm$  STD curves). In contrast, in [Figure S3B](#) we generate a single value the Synchrony Measure (or the other measures of interest) over the last 1000 ms of the simulation. [Figure S3B](#) displays this measure averaged over five independent simulations.

[Figure S3](#) includes the presentation of our Bifurcation Measure  $B$ . This quantifies the presence of sudden and significant changes in the Synchrony Measure over time. First, we take the Synchrony Measure time series for each independent run (i.e., as presented in [Figure 3](#)), and use the *smooth* function in MATLAB (MATLAB, 2019) with a 500 step window, generating a new time series from this moving average filter. This low-pass filter serves to account for fluctuations arising when, for example, a particular 100 ms window includes more or less activity than average. We denote this filtered time-series  $S_s$ . Second, we calculate the difference quotient  $\frac{\delta S_s}{\delta I}$ , where  $I$  is the value of the external drive (plotted against time in [Figure 3](#)), at each step in the time series. Finally, we take the variance of the values of  $\frac{\delta S_s}{\delta I}$  using the *var* function in MATLAB (MATLAB, 2019); networks in which the Synchrony Measure changes in a consistently linear fashion will have a tight distribution of  $\frac{\delta S_s}{\delta I}$  around the average slope (see, for example, [Figure 3B](#)), and thus a low variance; in contrast, networks in which the Synchrony Measure undergoes abrupt transitions will yield a multi-modal distribution of  $\frac{\delta S_s}{\delta I}$ , with each mode corresponding to different linear sections of  $S_s$ , and thus the variance of these values will be notably higher (see, for example, [Figure 3C](#)). The plotted value of  $B$  represents an average over the  $B$  values calculated for each independent network instantiation. We note that when we calculate the “firing rate Bifurcation Measure”  $B_e$  in reference to the four scenarios in [Figure 4](#), we simply replicate the above steps on the firing rate time series rather than the Synchrony Measure time series.

We emphasize that the Bifurcation Measure is appropriate for identifying the dynamics of interest in this work given that the related quantifications increase largely monotonically in response to increased drive, especially once these time series are “smoothed” prior to the application of this measure. The smoothed Synchrony Measure and firing rates do not display any discontinuous behaviors in our experimental paradigms that might confound this measure.

### Analysis of FI curves

In [Figure 5](#), we compare activation functions derived from experimental data with model analogues (i.e., the function  $F$  described below in [Equation 12](#)). In [Figure 5B](#) we show examples of  $F$  with epileptogenic and non-epileptogenic levels of heterogeneity alongside samples of the function  $f$  ([Equation 2](#)) randomly chosen based on the differing heterogeneity levels.

In [Figure 5A](#), we confirm the correspondence between the  $F$  functions and the experimental data by determining the value of  $\sigma_e$  best fitting this data. This process involved three steps: first, we qualitatively determined the portion of the  $F$  curves most likely to fit this data as that in  $-11.875 \leq U_e \leq -6.25$ ; second, both the  $U_e$  ( $[-11.875 -6.25]$ ) and probability of firing ( $[0.003585 .2118]$ ) variables were re-scaled to match the ranges exhibited by the input current (pA,  $[50 250]$ ) and firing frequency (Hz,  $[0 24]$ ) variables in the experimental data; finally, a fit was calculated using MATLAB’s (MATLAB, 2019) Curve Fitting application. This process used a non-linear least squares method, with  $r^2 > .93$  for both fits (see details in [Results](#)). Additional scaling was performed for plotting so that the two axes in [Figure 5](#) remain consistent.

### Modeling: Mean-field reduction

Following previous work (Hutt et al., 2016, 2020, 2020; Stefanescu et al., 2012; Hutt et al., 2020; Rich et al., 2020b; Lefebvre et al., 2015) we perform a mean-field reduction of the spiking network in [Equation 3](#). We assume that the firing rate of cells is sufficiently high to make use of the diffusion approximation (Gluss, 1967), yielding

$$\alpha_e^{-1} \frac{dU_e}{dt} = -U_e + w_{ee} F(U_e, \sigma_e) + w_{ie} F(U_i, \sigma_i) + I_e^0 + I_e(t) \quad (\text{Equation 10})$$

$$\alpha_i^{-1} \frac{dU_i}{dt} = -U_i + w_{ii} F(U_i, \sigma_i) + w_{ei} F(U_e, \sigma_e) + I_i^0 \quad (\text{Equation 11})$$

where  $U_{e,j} = \frac{1}{N_{e,i}} \sum_{j=1}^{N_{e,j}} U_{e,j}$  represents the mean activity of the excitatory or inhibitory population, respectively.

The function  $F$  represents the average activation function conditioned upon the value of  $\sigma_{e,j}$  via the convolution

$$F(U_{e,j}, \sigma_{e,j}) = \int_{-\infty}^{\infty} f(U_{e,j} + v, 0) \rho(v) dv \quad (\text{Equation 12})$$

where  $\rho(v) = N(0, \sigma_{e,j}^2)$  (Lefebvre et al., 2015; Hutt et al., 2016, 2018).

### Linear stability analysis of the mean-field equations

Fixed points  $\bar{U}_{e,j}$  of the mean-field equations satisfy

$$0 = -\bar{U}_e + w_{ee}F(\bar{U}_e, \sigma_e) + w_{ie}F(\bar{U}_i, \sigma_i) + I_e^o + I_e(t) \quad (\text{Equation 13})$$

$$0 = -\bar{U}_i + w_{ii}F(\bar{U}_i, \sigma_i) + w_{ei}F(\bar{U}_e, \sigma_e) + I_i^o \quad (\text{Equation 14})$$

Linearizing about the steady state values of  $\bar{U}_{e,j}$  yields the system

$$\frac{d}{dt} \begin{pmatrix} \delta \bar{U}_e \\ \delta \bar{U}_i \end{pmatrix} = \mathbf{A} \begin{pmatrix} \delta \bar{U}_e \\ \delta \bar{U}_i \end{pmatrix} = \begin{pmatrix} -\alpha_e + w_{ee}\alpha_e R_e & w_{ie}\alpha_e R_i \\ w_{ei}\alpha_i R_e & -\alpha_i + w_{ii}\alpha_i R_i \end{pmatrix} \begin{pmatrix} \delta \bar{U}_e \\ \delta \bar{U}_i \end{pmatrix} \quad (\text{Equation 15})$$

with  $R_{e,j} = R(\bar{U}_e, \bar{U}_i) = \int_{-\infty}^{\infty} f'[\bar{U}_{e,j} + v, 0] \rho(v) dv$ . The system's stability is given by the eigenvalues of the Jacobian  $\mathbf{A}$ . Define

$$B = \text{trace}(\mathbf{A}) = -(\alpha_e + \alpha_i) + (w_{ee}\alpha_e)R_e + (w_{ii}\alpha_i)R_i \quad (\text{Equation 16})$$

$$C = \det(\mathbf{A}) = (-\alpha_e + (w_{ee}\alpha_e)R_e)(-\alpha_i + (w_{ii}\alpha_i)R_i) - ((w_{ie}\alpha_e)R_i)((w_{ei}\alpha_i)R_e) \quad (\text{Equation 17})$$

Eigenvalues of  $\mathbf{A}$  are thus given by

$$\lambda_{\pm} = \frac{1}{2} \left( B \pm \sqrt{B^2 - 4C} \right) \quad (\text{Equation 18})$$

### Bifurcation analysis with varying excitatory input

We investigate bifurcation properties as a function of  $I_e(t)$ . In Figure S3A, multi-stability, as denoted by the bold border, is determined by testing for the presence of multiple fixed points at  $I_e(t)$  ranging from 0:0.625:9.375, a range encompassing the range for multi-stability shown in Figure 4.

### QUANTIFICATION AND STATISTICAL ANALYSIS

Plotting of experimental data was performed using GraphPad Prism 6 (GraphPad software, Inc, CA, USA). The non-parametric Mann-Whitney test was used to determine statistical differences between the means of two groups. The F-test was used to compare standard deviation (SD) between groups. The two sample coefficient of variation test was used to compare the coefficient of variance (CV) between groups. Normality of the data was tested with the Shapiro-Wilk and D'Agostino - Pearson omnibus normality tests with  $\alpha = 0.05$ . The one-way ANOVA post hoc with Dunn's multiple comparison test was used to determine statistical significance in the spike frequency adaptation ratio. A standard threshold of  $p < 0.05$  is used to report statistically significant differences.

Statistical details can be found in the relevant section of the Results and/or the figure legends. Reported values of  $n$  refer to the number of cells recorded.